Mesoscale Predictability in Moist Midlatitude Cyclones Is Not Sensitive to the Slope of the Background Kinetic Energy Spectrum

DANIEL J. LLOVERAS,[a] LYDIA H. TIERNEY,[a] AND DALE R. DURRAN[a]

[a]*Department of Atmospheric Sciences, University of Washington, Seattle, Washington*

(Manuscript received 26 May 2021, in final form 21 October 2021)

ABSTRACT: We investigate the sensitivity of mesoscale atmospheric predictability to the slope of the background kinetic energy spectrum E by adding initial errors to simulations of idealized moist midlatitude cyclones at several wavenumbers k for which the slope of $E(k)$ is significantly different. These different slopes arise from 1) differences in the $E(k)$ generated by cyclones growing in two different moist baroclinically unstable environments, and 2) differences in the horizontal scale at which initial perturbations are added, with $E(k)$ having steeper slopes at larger scales. When small-amplitude potential temperature perturbations are added, the error growth through the subsequent 36-h simulation is not sensitive to the slope of $E(k)$ nor to the horizontal scale of the initial error. In all cases with small-amplitude perturbations, the error growth in physical space is dominated by moist convection along frontal boundaries. As such, the error field is localized in physical space and broad in wavenumber (spectral) space. In moist midlatitude cyclones, these broadly distributed errors in wavenumber space limit mesoscale predictability by growing up-amplitude rather than by cascading upscale to progressively longer wavelengths. In contrast, the error distribution in homogeneous turbulence is broad in physical space and localized in wavenumber space, and dimensional analysis can be used to estimate the error growth rate at a specific wavenumber k from $E(k)$. Predictability estimates derived in this manner, and from the numerical solutions of idealized models of homogeneous turbulence, depend on whether the slope of $E(k)$ is shallower or steeper than k^{-3}, which differs from the slope-insensitive behavior exhibited by moist midlatitude cyclones.

KEYWORDS: Extratropical cyclones; Mesoscale processes; Baroclinic models; Numerical weather prediction/forecasting

1. Introduction

Lorenz (1969) suggested that certain flows with many scales of motion, such as the atmosphere, may have a finite predictability limit that cannot be extended by decreasing initial errors to any magnitude greater than zero. In Lorenz's model, which represents two-dimensional homogeneous turbulence, error growth is dominated by a cascade from small to large scales, and this upscale cascade is dependent on the slope of the flow's background kinetic energy (KE) spectrum $E(k)$ where k is the horizontal wavenumber. If $E(k)$ is proportional to k^{-p} for $p < 3$, the upscale error cascade proceeds faster on progressively smaller scales, and any nonzero initial error will produce a complete loss in predictability in a finite time. In contrast, if $p \geq 3$, the upscale error transfer does not become progressively faster at smaller scales, so predictability can be extended indefinitely by continually reducing the initial-error scale and amplitude. Lorenz's "butterfly effect" has been supported by studies using more advanced turbulence models (Leith and Kraichnan 1972; Métais and Lesieur 1986; Rotunno and Snyder 2008) and is now a widely accepted concept in dynamic meteorology.

However, the extent to which error-growth estimates from homogeneous turbulence apply to atmospheric predictability is not well understood. Even so, the background KE spectrum in the atmosphere does tend to follow power laws similar to those assumed for $E(k)$ in the aforementioned idealized studies. Observations have shown that in the midlatitudes, the time-averaged $E(k)$ approximately follows a k^{-3} power law on synoptic scales, while at mesoscale wavelengths less than about 400 km, the slope gradually shallows to $k^{-5/3}$ (Nastrom and Gage 1985). Similar background KE spectra have been produced using realistic global convection-permitting numerical simulations (Skamarock et al. 2014; Judt 2018). Following turbulence theory, the $k^{-5/3}$ slope of $E(k)$ on the mesoscale suggests that the atmosphere should have finite predictability. Indeed, studies using full-physics atmospheric models have agreed with Lorenz's estimate that midlatitude synoptic-scale weather systems have an intrinsic predictability limit of about 2 weeks (Zhang et al. 2019; Judt 2020). The possibility of improving the applicability of turbulence theory to the atmosphere has motivated the development of turbulence models with hybrid k^{-3} and $k^{-5/3}$ KE spectra (Durran and Gingrich 2014; Sun and Zhang 2020; Leung et al. 2020).

Vigorous atmospheric convection provides one important path for errors to propagate through the mesoscale and ultimately limit the predictability on all scales. Selz and Craig (2015) showed that error growth in a simulation of a real summertime weather event proceeded most rapidly in regions of strong, precipitating convection. Sun and Zhang (2016, hereafter SZ16) investigated error growth in idealized simulations of moist midlatitude cyclones with strong convective instability. They concluded that "the short-range forecast is dominated by the upscale growth from the small scales" due to moist convection and that "the predictability behavior is closely linked to the flow's kinetic energy spectrum," as is the case in homogeneous turbulence. Nevertheless, spectral error growth in convection-permitting simulations of realistic

Corresponding author: Daniel J. Lloveras, lloveras@uw.edu

DOI: 10.1175/JAS-D-21-0147.1

atmospheric flows is typically different from the way small-scale errors evolve in turbulence models. In realistic flows the errors tend to grow uniformly at all scales in an "up-amplitude" fashion, rather than via an upscale cascade from the shortest wavelengths (Mapes et al. 2008; Durran et al. 2013; Durran and Gingrich 2014; Selz and Craig 2015; Weyn and Durran 2017; Judt 2018, 2020).

The main goal of this paper is to investigate the sensitivity of atmospheric predictability to the initial-error scale and to the slope of the background KE spectrum. We conduct our experiments using convection-permitting idealized simulations of isolated midlatitude cyclones developing within moist baroclinically unstable channels, as in several previous predictability studies (Zhang et al. 2007; Bei and Zhang 2014; SZ16). Similarly to those studies, we will focus on error growth through the mesoscale at lead times up to 36 h, since baroclinic-wave channel simulations lack the planetary-scale circulations that would need to be included in realistic simulations of error growth on synoptic and larger scales over longer lead times. Our strategy is to perturb the potential temperature fields in our simulations at distinct wavelengths and amplitudes and compare the evolution of the perturbed and unperturbed runs.

The remainder of this paper is organized as follows. In section 2 we introduce the baroclinic-wave simulations used to run our predictability experiments: one following that of SZ16 and another that simulates moist processes more realistically. Section 3 outlines the initial perturbation strategy. We discuss error growth in physical space in section 4 and error growth in spectral space in section 5. We provide concluding remarks in section 6.

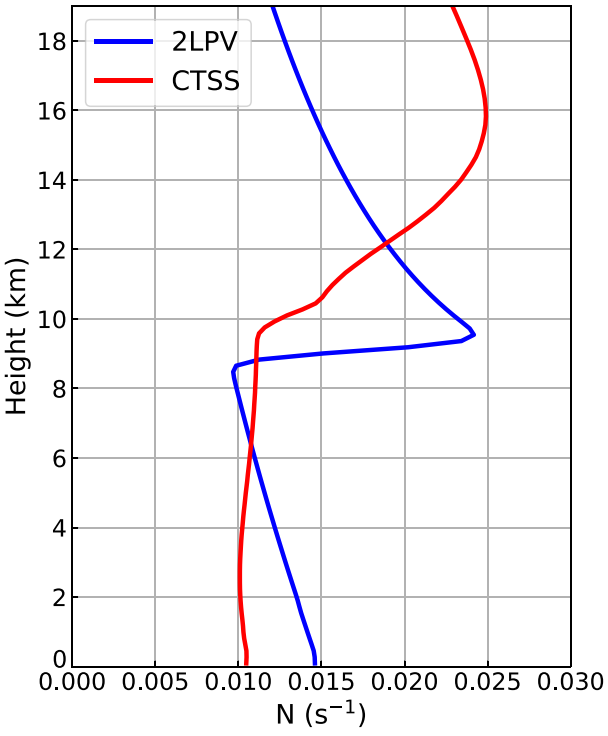

FIG. 1. Vertical profiles of buoyancy frequency N (s^{-1}) for the 2LPV (blue) and CTSS (red) background states. The profiles of N are zonally averaged in the meridional center of the respective domains (y = 4000 km for the 2LPV simulation and y = 3600 km for the CTSS simulation).

2. Overview of the simulations

a. Model configuration

We use the Advanced Research version of the Weather Research and Forecasting Model (WRF-ARW version 3.6.1; Skamarock et al. 2008) to run idealized simulations of moist baroclinic waves in f-plane channels with zonally periodic and meridionally symmetric boundaries. The background state for the simulations is a zonally uniform jet profile that we generate by inverting a potential vorticity (PV) field in the y–z plane following Rotunno et al. (1994). The horizontal grid resolution is Δx = 4 km, which is well within the range of grid spacings used in typical convection-permitting simulations, but is nevertheless too coarse to accurately resolve the true scale of convective updrafts. The errors in ensemble and near-twin simulations of systems with deep convection would be expected to grow more rapidly if the resolution were improved (Weyn and Durran 2018). There are 100 vertical levels with the model top at 20 km.

We configure our first family of simulations following SZ16; the background-state PV is a constant 0.4 potential vorticity units (PVU; 1 PVU = 10^{-6} K m^2 s^{-1} kg^{-1}) in the troposphere and a constant 4 PVU in the stratosphere, with PV increasing sharply within the tropopause. We call the simulations using this setup the "two-layer potential vorticity" (2LPV) simulations. The 2LPV approach is a widely used method for generating background states for idealized baroclinic-wave simulations (Rotunno et al. 1994; Tan et al. 2004; Zhang et al. 2007; Menchaca and Durran 2017).

However, the 2LPV simulations develop unrealistic vertical motions because the background-state static stability profile in the troposphere is unrealistic. Holding PV constant within the troposphere forces $\partial\bar{\theta}/\partial z$ to decrease with height, since the background density $\bar{\rho}(z)$ decreases with height and Ertel's PV is PV = $(\zeta_a \cdot \nabla\theta)/\rho$. This, combined with the fact that θ increases with height, causes the buoyancy frequency $N^2 = (g/\theta)(d\bar{\theta}/dz)$ to decrease with height. As shown by the blue curve in Fig. 1, prescribing constant PV in the troposphere thus results in unrealistically high buoyancy frequency near the surface (almost 0.015 s^{-1}) and more realistic values of N just below the tropopause (about 0.01 s^{-1}). We will show in section 2b that this unrealistic profile of N leads to anomalous wave activity at low levels and unrealistic moist convection confined to the upper troposphere. Since moist processes have been shown to play a key role in modulating error growth in baroclinic waves (Zhang et al. 2007; SZ16), the results of our predictability experiments using the 2LPV simulations are likely limited to flows with similar degrees of convective instability and wave activity.

To address this issue, we consider a second family of baroclinic-wave simulations in which the background-state

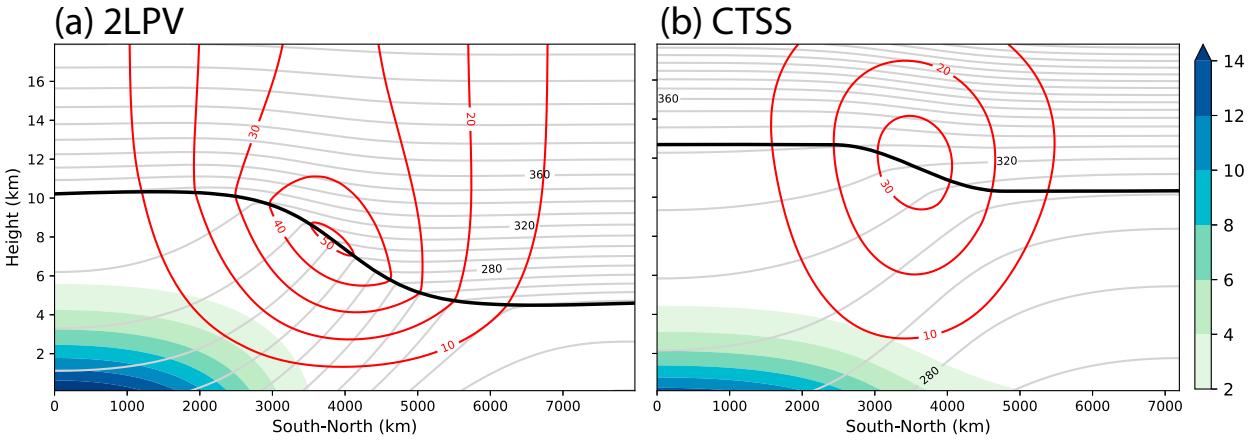

FIG. 2. South–north vertical cross sections of the (a) 2LPV and (b) CTSS background states for zonal wind (red contours every 10 m s^{-1}), potential temperature (gray contours every 10 K), and water vapor mixing ratio (color fill every 2 g kg^{-1}, as denoted by the color bar). The tropopause is represented by the thick black line, which refers to where the potential vorticity is equal to 1.5 PVU in the 2LPV simulation and 1.8 PVU in the CTSS simulation.

buoyancy frequency is roughly a constant 0.01 s^{-1} throughout the troposphere (as shown by the red curve in Fig. 1). We designate these simulations the "constant tropospheric static stability" (CTSS) simulations. We create the simple, but more realistic thermodynamic structure of the CTSS background state by prescribing a PV field that increases with height within both the troposphere and the stratosphere. The PV at the bottom of the troposphere is 0.22 PVU and the PV at the bottom of the stratosphere is 1.8 PVU. We outline the details of this PV field in appendix A, and we invert the field using the same methodology as in the 2LPV case.

Figure 2 depicts the background-state jet profiles for the 2LPV and CTSS simulations. The 2LPV jet closely resembles that of SZ16 (their Fig. 1), with a zonal wind maximum of just over 50 m s^{-1} at a height of about 8 km, a meridional surface temperature gradient of about 70 K, and a tropopause height that ranges from about 10 km in the south to 5 km in the north. In contrast, the CTSS tropopause height ranges from about 13 to 10 km, which is more consistent with observations at midlatitudes than in the 2LPV case (Kishore et al. 2006). The higher and more gently sloped CTSS tropopause is also associated with a weaker jet maximum (about 35 m s^{-1}) at about 12-km height and a weaker meridional surface temperature gradient (about 30 K) than in the 2LPV background state. The 2LPV and CTSS moisture fields have similar structures, although the CTSS water vapor mixing ratio values are smaller, extend farther north, and do not extend as high up in the atmosphere. Note that we compute the 2LPV moisture field following the relative humidity formula in SZ16 (their appendix A), while we calculate the CTSS water vapor mixing ratios using the formula in appendix B.

The 2LPV and CTSS simulations also have different domain sizes and parameterizations. The 2LPV domain is the same size as in SZ16, with a zonal extent of $L_x = 4000$ km and a meridional extent of $L_y = 8000$ km, although the 4-km horizontal resolution is an improvement upon the 10-km resolution used in SZ16. The CTSS domain is twice as long in the zonal direction, with $L_x = 8000$ km and $L_y = 7200$ km, to allow the cyclone more room to develop away from the periodicity constraint at the zonal boundaries. The 2LPV parameterizations follow those of SZ16; we use the Lin et al. (1983) microphysics scheme, the Hong and Pan (1996) planetary boundary layer scheme, and the Monin–Obukhov similarity theory to parameterize surface layer friction with the default roughness of $z_0 = 0.01$ m (fluxes of heat and moisture are set to zero). The CTSS parameterizations are selected based on the default WRF schemes; we use the Yonsei University (YSU) planetary boundary layer scheme (Hong et al. 2006) and the revised surface layer scheme based on the fifth-generation Pennsylvania State University–National Center for Atmospheric Research Mesoscale Model (MM5) parameterization (Jiménez et al. 2012). Although it is not the default, we use the National Severe Storms Laboratory (NSSL) two-moment microphysics scheme (Mansell et al. 2010) for the CTSS simulation because two-moment schemes have been shown to have significant advantages over one-moment schemes (Johnson and Jung 2016). In both simulations, we use the Rayleigh damping scheme described in Klemp et al. (2008) in the top 5 km of the model, we do not include solar nor infrared radiation, and we do not use cumulus parameterization.

b. Cyclone evolution

We generate the 2LPV and CTSS cyclones using a method similar to that of Menchaca and Durran (2017). Cyclone growth is triggered by a localized quasigeostrophic PV anomaly of the form

$$Q'(x,y,z) = Q_0 e^{-\left(s/\delta_h\right)^2} e^{-\left[(z-z_c)/\delta_v\right]^2}, \tag{1}$$

where $s^2 = (x - x_c)^2 + (y - y_c)^2$, the magnitude is $Q_0 = 3.0 \times 10^{-5}$ s^{-1}, and the decay scales are $\delta_h = 1000$ km in the horizontal and $\delta_v = 3$ km in the vertical. The center of the 2LPV anomaly is located at $(x_c, y_c, z_c) = (1000, 3000, 6.5$ km),

placing it below and to the south of the jet maximum. We choose the same y–z location for the CTSS anomaly, except we change the zonal center to $x_c = 2400$ km in light of the larger zonal domain to ensure that the anomaly is well away from the periodic boundary. After seeding the cyclone, the model is integrated for 24 h using the WRF Dolph–Chebyshev digital filter (Lynch 1997) to remove any artificial gravity waves of periods less than 6 h caused by imbalances in the initial state. The filtered variables serve as the new initial conditions at 12 h into the simulation, from which the standard, unfiltered WRF Model is integrated forward.

As in SZ16, we consider the growth of potential temperature perturbations in our baroclinic-wave simulations over 36-h forecast periods. In the 2LPV experiments, we add the perturbations at day 4.5 of the simulation, at which time the cyclone is in roughly the same developmental stage as the cyclone in SZ16 when they added perturbations to their simulations. The main period of focus for the CTSS experiments (3–4.5 days) covers an earlier stage of baroclinic growth in which the cyclone deepens more rapidly than in the 2LPV case (Fig. 3). As will be discussed (in connection with Fig. 13), the error growth over this 3–4.5-day period of rapid deepening is nevertheless similar to that which occurs if perturbations are added to the CTSS simulation at 4.5 days.

Figure 3 shows the 2LPV and CTSS surface temperature and pressure fields at 12 and 36 h after the addition of perturbations. The CTSS cyclone is significantly more realistic than the 2LPV cyclone. The CTSS cyclone closely resembles the Norwegian cyclone model first introduced by Bjerknes (1919), with distinct warm, cold, and occluded fronts and cold air that wraps around the low pressure center as the cyclone matures. In contrast, cold air does not wrap around the 2LPV cyclone as it deepens and moves northward, resulting in the development of a large region with a weak surface temperature gradient just south of the low pressure center. By 36 h the 2LPV cyclone has developed unrealistic kinks in the surface pressure and temperature fields on scales of about 100 km (Fig. 3b); this is consistent with the surface features found in the simulations of Tan et al. (2004) and Zhang et al. (2007) that use a similar background state.

Figure 4 shows how the improved tropospheric static stability profile in the CTSS simulation leads to more realistic clouds and moist convection than in the 2LPV case. Figures 4a and 4b show the cloud-top temperature fields for the two simulations (at day 5 for 2LPV, day 4.5 for CTSS). The 2LPV cloud field is dominated by low, warm clouds, many with wavelike structures, particularly in the warm sector and cloud shield. The majority of the coldest cloud tops are convective clouds that occur sporadically along the cold front. In contrast, the CTSS cloud field is much more robust and realistic, as the clouds extend high into the atmosphere and are structured in a way that reflects the large-scale rising motions that are characteristic of midlatitude cyclones.

The cross sections of vertical velocity and potential temperature in Figs. 4c and 4d correspond to the locations of the red lines in Figs. 4a and 4b, respectively. In the 2LPV cross section, the anomalously high near-surface static stability confines low-level vertical motion to wavelike features with wavelengths of about 40 km, while convective cells develop in the 6–10-km layer where the buoyancy frequency is approximately 0.01 s^{-1} (Fig. 1). In contrast, the vertical motion in the CTSS cross section is dominated by large-scale ascent along the cyclone's warm conveyor belt. Also, the region of higher vertical velocity in the western portion of the CTSS cross section is associated with snowfall. These broader features in the vertical velocity field are more representative of rising motions in the cloud fields of real-world midlatitude cyclones.

c. *Background KE spectra*

We compute two-dimensional (2D) KE spectra for the 2LPV and CTSS simulations following Menchaca and Durran (2019). First, we interpolate the WRF data onto constant-height surfaces with 200 m vertical intervals. Next, we extend the variables periodically in the meridional direction following Waite and Snyder (2013) to create a doubly periodic domain of size L_x by $2L_y$, taking advantage of the periodic boundary conditions in x and the symmetric boundary conditions in y. We then compute Fourier transforms of the velocity fields using the default option in Python's numpy.fft module. Denoting the 2D discrete Fourier transform of a function ϕ by $\hat{\phi}$ and its complex conjugate by $\hat{\phi}^*$, we compute the density-weighted KE spectral density at each vertical level m using the binning technique described in Durran et al. (2017) as

$$E_m(k_p) = \frac{\bar{\rho}_m \Delta x \Delta y \, \min(\Delta k_x, \Delta k_y)}{8\pi^2 N_x N_y} \sum_{\mathbf{k}\in R(p)} [\hat{u}_m(\mathbf{k})\hat{u}_m^*(\mathbf{k}) + \hat{v}_m(\mathbf{k})\hat{v}_m^*(\mathbf{k})], \tag{2}$$

where $\bar{\rho}(z)$ is a horizontally uniform background density profile, $\Delta x = \Delta y = 4$ km is the horizontal grid spacing, N_x and N_y are the numbers of grid points in the zonal and meridional directions, respectively, $\mathbf{k} = (k_x, k_y)$ is the horizontal wavenumber vector, and $\Delta k_x = 2\pi/L_x$ and $\Delta k_y = 2\pi/L_y$ are the zonal and meridional wavenumber spacings, respectively. To define $R(p)$, we discretize the 2D wavenumber in multiples of the maximum one-dimensional wavenumber $\Delta k_h = \max(\Delta k_x, \Delta k_y)$ such that $k_p = p\Delta k_h$, $p = 1, 2, \ldots, N_{\max}$, where $N_{\max} = \left\lceil \sqrt{2}\max(N_x/2, N_y/2) \right\rceil$. Then $R(p)$ is the set of wavenumber indices $\mathbf{k} = (k_x, k_y)$ satisfying $k_p - \Delta k_h/2 \le \sqrt{k_x^2 + k_y^2} \le k_p + \Delta k_h/2$.

Figure 5 shows $E(k)$ for the unperturbed 2LPV and CTSS simulations at the time we add the perturbations and 36 h after. The red curves correspond to the midtroposphere, which we define as the 2–6-km vertical range in the 2LPV simulation and 4–8 km for the CTSS case. The blue curves correspond to the lower stratosphere, which we define as 8–12 km in the 2LPV simulation and 10–14 km for the CTSS case.

At mesoscale wavenumbers, the 2LPV and CTSS simulations exhibit dramatically different $E(k)$. The slopes of the mesoscale 2LPV spectra are shallower than the canonical $k^{-5/3}$ power law at both levels and times; in fact, the tropospheric spectra are consistently flat at wavelengths between

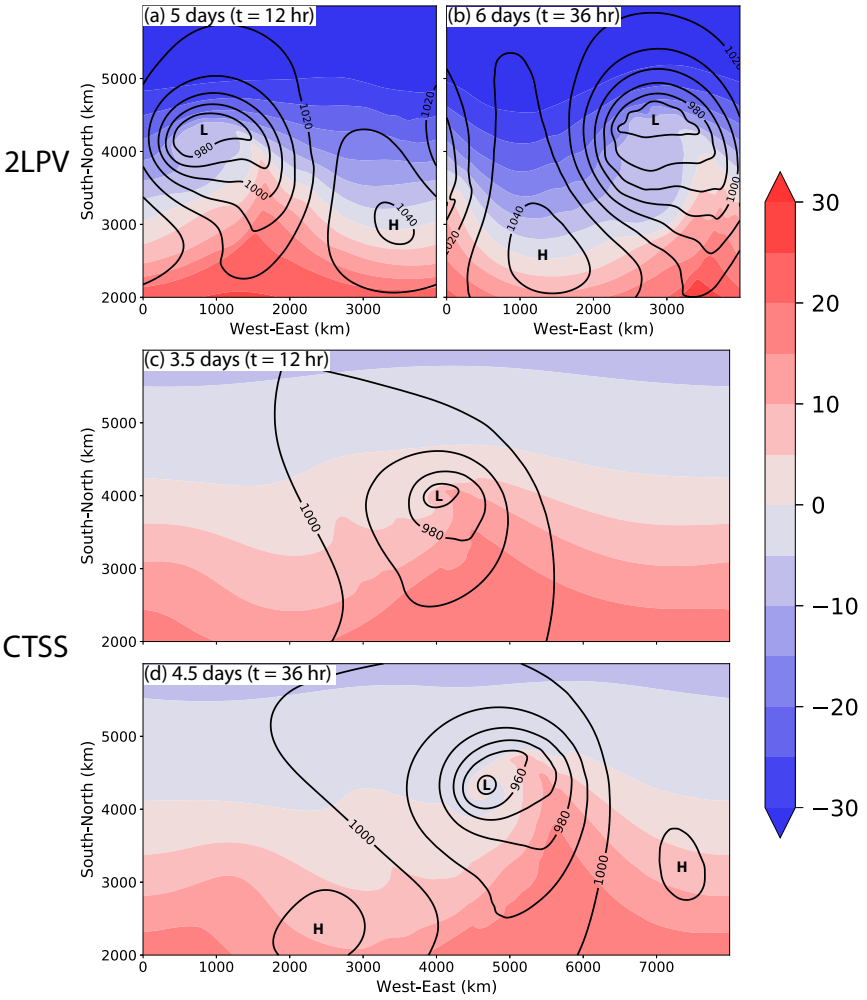

FIG. 3. Surface pressure (black contours every 10 hPa) and surface temperature (color fill every 5°C, as denoted by the color bar) for the unperturbed (a),(b) 2LPV and (c),(d) CTSS cyclones at (a),(c) 12 and (b),(d) 36 h after the initial perturbations are added. Lows and highs are labeled by "L" and "H," respectively.

40 and 80 km. This is in stark contrast to the CTSS spectra in the mesoscale, which have slopes that are steeper than $k^{-5/3}$ at both levels and times and more closely follow a k^{-2} power law. Previous studies have indicated that moist convection and gravity waves are often responsible for energizing the mesoscale (Sun et al. 2017; Weyn and Durran 2017; Menchaca and Durran 2019), so it is likely that the dramatic differences in the mesoscale energy spectra in the 2LPV and CTSS simulations are due to the more prominent wave activity in the 2LPV case (see Fig. 4).

At scales greater than 400 km, both the 2LPV and CTSS spectra approximately follow a k^{-3} power law in the troposphere and have slightly steeper slopes in the stratosphere. In addition, $E(k)$ increases with time in both simulations and at all scales and levels as the cyclones develop. Nevertheless, the spectral slopes are generally constant in time, except in the 2LPV stratosphere, where the mesoscale spectrum flattens and the large-scale spectrum smoothens during the 36-h forecast period.

The stark differences between the 2LPV and CTSS mesoscale KE spectra offer an opportunity to assess the sensitivity of mesoscale atmospheric predictability to the slope of $E(k)$. The remainder of this paper focuses on how errors of varying initial scales and amplitudes grow over 36-h forecast periods in the 2LPV and CTSS baroclinic-wave simulations.

3. Design of the perturbations

The potential temperature perturbations added at day 4.5 of the 2LPV simulation and day 3 of the CTSS simulation are of the form

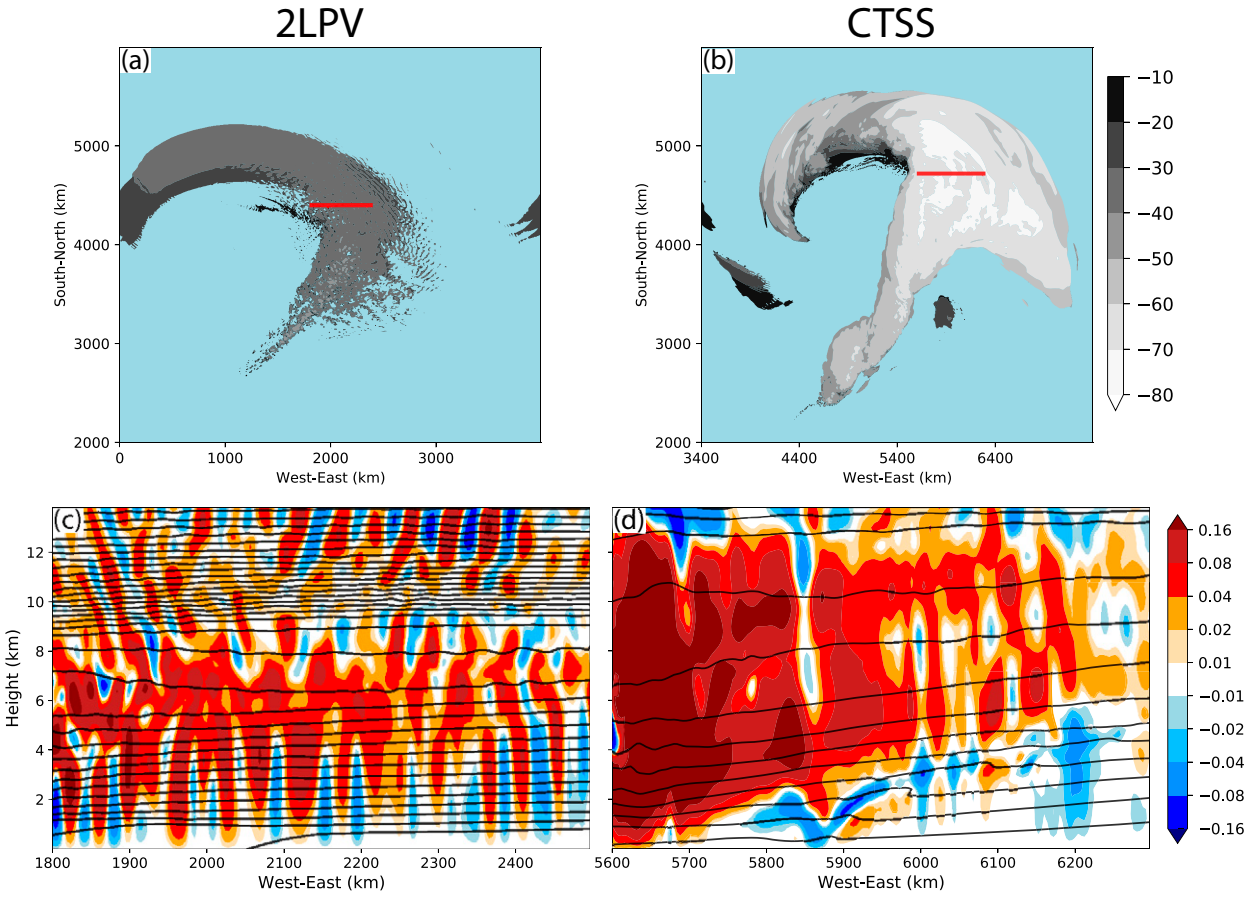

FIG. 4. (a),(b) Cloud-top temperature (gray-scale fill every 10°C, as denoted by the color bar) and (c),(d) east–west vertical cross sections of vertical velocity (color fill, in m s^{-1}, as denoted by the nonlinear color bar) and potential temperature (black contours every 4 K) at (a),(c) day 5 of the unperturbed 2LPV simulation and (b),(d) day 4.5 of the unperturbed CTSS simulation. The red lines in (a) and (b) correspond to the respective locations of the cross sections in (c) and (d).

$$\theta'(x,y,z) = Ae^{-z/H}\sin\left[2\pi\left(\frac{x}{L}-\phi_x\right)\right]\sin\left[2\pi\left(\frac{y}{L}-\phi_y\right)\right], \quad (3)$$

where A is the amplitude, L is the horizontal scale, and $H = 1$ km is the e-folding height scale. We use this monochromatic perturbation structure to isolate the effects of errors at specific scales. This allows for a clearer distinction between upscale and downscale error propagation than the errors in SZ16, which were added over ranges of wavelengths and had different structures at large and small scales. We add the perturbations at three amplitudes $A = 0.01$, 0.1, and 1.0 K and three horizontal scales $L = 24$, 400, and 1000 km. For the 2LPV experiments, we use the random phase shifts ϕ_x and ϕ_y ($0 \le \phi_{x,y} \le 2\pi$) to generate 5 ensemble members at each scale and amplitude. We do not run ensembles for the CTSS experiments due to the computational limitations of the larger CTSS domain. Instead, we set $\phi_x = \phi_y = 0$ for the perturbed runs, resulting in near-twin simulations.

The black symbols plotted on the KE spectra in Fig. 5 mark the initial wavelengths of these perturbations. Note that a perturbation at scale L in (3) has a 2D wavelength of $2^{-1/2}L$. We choose $L = 24$ km as the smallest-scale perturbation (indicated by the triangles in Fig. 5) because it is roughly the shortest wave that is not significantly damped by numerical dissipation. We choose $L = 400$ km as the medium-scale perturbation (indicated by the circles in Fig. 5) because it represents a transition point between the shallower mesoscale KE spectra and steeper slopes in the synoptic scales. We choose $L = 1000$ km as the largest-scale perturbation (indicated by the squares in Fig. 5) because it lies among the synoptic scales where the KE spectral slopes are approximately k^{-3} and fits easily within our domain.

We choose the perturbation amplitude $A = 0.1$ K to approximately match the magnitude of the perturbations in SZ16. We decrease this amplitude by a factor of 10 for the 0.01-K experiments to see if our simulations have limited predictability and to evaluate the importance of initial scale as errors become smaller in magnitude. We increase the 0.1-K amplitude by a factor of 10 for the 1.0-K experiments to examine how growth dynamics and initial-scale sensitivities change as errors become larger in magnitude.

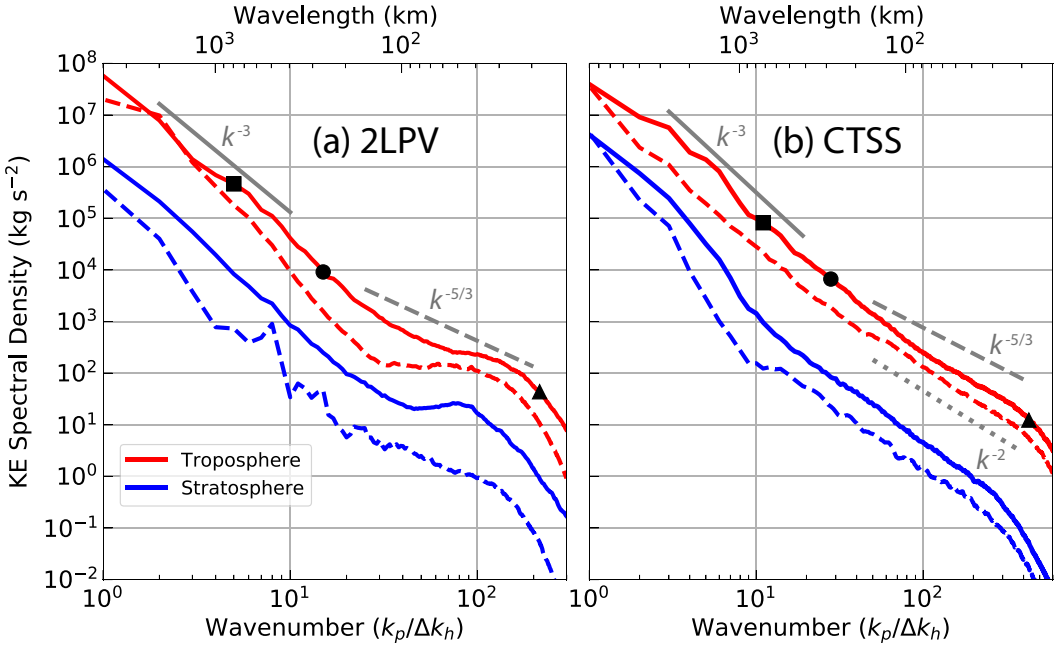

FIG. 5. Two-dimensional background kinetic energy (KE) spectral densities (kg s^{-2}) for the (a) 2LPV and (b) CTSS simulations. Spectra are plotted at the time the initial errors are added (dashed) and 36 h after (solid) and are vertically averaged over the midtroposphere (red) and lower stratosphere (blue). Stratospheric spectra are shifted down by a factor of 10 for visibility. Gray lines with slopes of k^{-3} (solid), $k^{-5/3}$ (dashed), and k^{-2} (dotted) are plotted for reference. The triangles, circles, and squares plotted on the 36-h tropospheric spectra indicate the 2D wavenumbers of the initial 24-, 400-, and 1000-km-scale perturbations, respectively.

As in SZ16, we use the difference total energy (DTE; $m^2\ s^{-2}$) as an error metric, which is defined at any grid point and time as

$$\mathrm{DTE} = \frac{1}{2}\left[(\delta u)^2 + (\delta v)^2 + \kappa(\delta T)^2\right], \tag{4}$$

where δu, δv, and δT are the differences between the unperturbed and perturbed fields of zonal wind, meridional wind, and temperature, respectively. The constant $\kappa = c_p/T_r$, where $c_p = 1004\ \mathrm{J\ K^{-1}\ kg^{-1}}$ is the specific heat at constant pressure and $T_r = 270$ K is a reference temperature.

4. Error growth in physical space

Figures 6 and 7 show the domain-integrated DTE time series for the 2LPV and CTSS experiments, respectively, displayed on a semilog plot to show the error growth at early times (Figs. 6a–c, 7a–c) and using a linear ordinate to capture the growth at later times (Figs. 6d–f, 7d–f). The time series for the 2LPV experiments are plotted for both the individual ensemble members (dotted) and the ensemble means of those DTE values (solid). The dashed lines in Figs. 7b and 7e correspond to two 0.1-K experiments using the CTSS environment without moisture.

In the 0.1-K experiments for both the 2LPV (Figs. 6b,e) and CTSS simulations (Figs. 7b,e), the total error growth is nearly independent of the initial scale throughout the 36-h forecast period. In the first 9 h, errors rapidly increase by nearly two orders of magnitude and grow slightly faster if the perturbations are smaller in scale (Figs. 6b and 7b). Throughout the remainder of both simulations, the sensitivity of the error to the initial scale is negligible.

The insensitivity to the initial scale is even more pronounced in the smallest-amplitude 0.01-K experiments (Figs. 6a,d and 7a,d); all curves lie on top of each other in both the linear and semilog plots. In addition, the DTE values in the 0.01-K experiments are nearly identical to those of the 0.1-K experiments after about 9 h. This suggests that our baroclinic-wave simulations have finite predictability, as reducing the initial amplitude by a factor of 10 does not reduce the total error growth through 36-h lead times.

Our result that the growth of small-amplitude perturbations is not sensitive to the initial scale is consistent with previous work (Lorenz 1969; Durran and Gingrich 2014; SZ16; Weyn and Durran 2017). However, recall that we add the perturbations not only at different spatial scales, but also at wavenumbers where the slope of the background KE spectrum is significantly different (Fig. 5). Thus, a key implication of our result that was not considered by the aforementioned studies is that error growth is not sensitive to the slope of the background KE spectrum at the wavelength of the initial perturbation.

In the largest-amplitude 1.0-K experiments (Figs. 6c,f and 7c,f), the error growth is different from the 0.01- and 0.1-K experiments in two key ways. First, the 36-h error growth

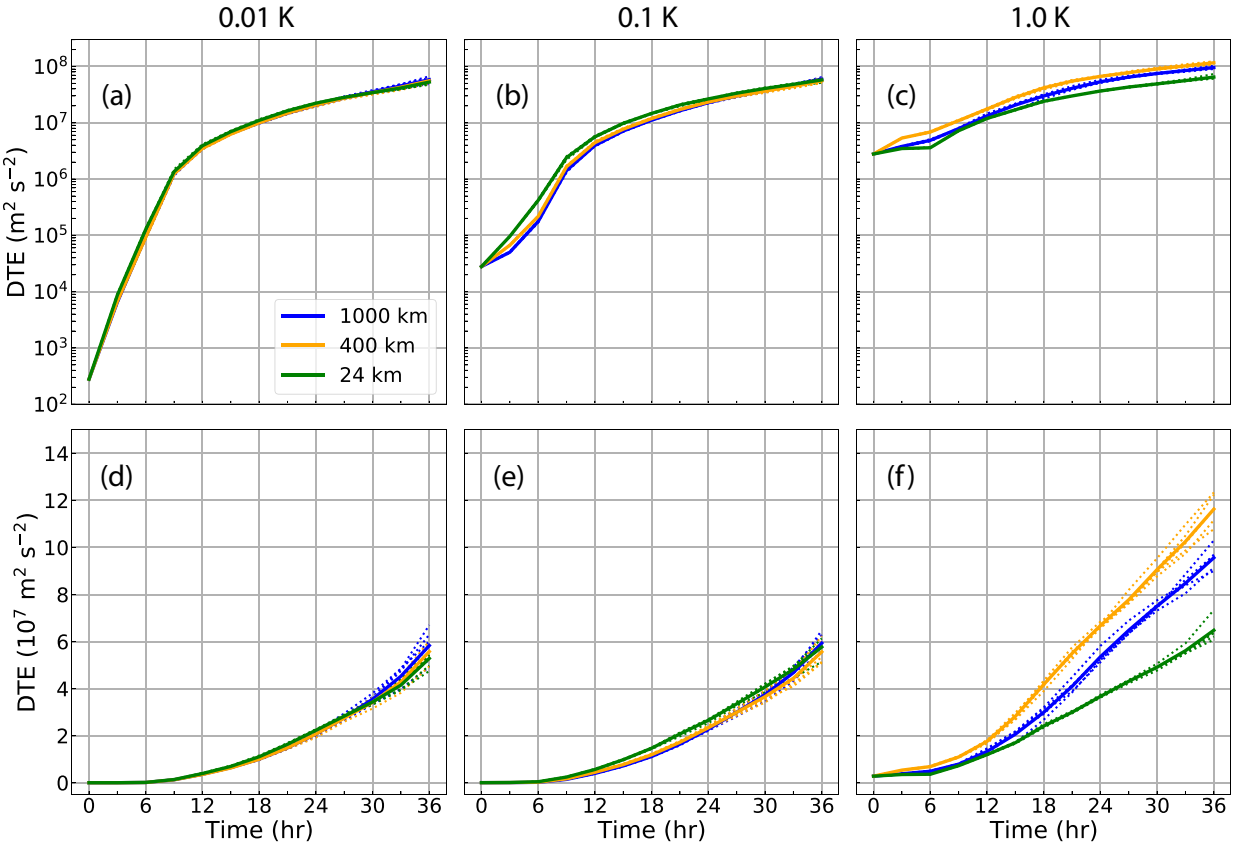

FIG. 6. Time series of the domain-integrated difference total energy (DTE; $m^2\ s^{-2}$) for the 2LPV experiments. DTE time series for the individual ensemble members (dotted) and the ensemble means of those DTE values (solid) are plotted for initial-error scales of 24 (green), 400 (orange), and 1000 (blue) km and initial-error amplitudes of (a),(d) 0.01, (b),(e) 0.1, and (c),(f) 1.0 K. In (a)–(c) DTE are plotted with a logarithmic *y* axis, while in (d)–(e) DTE are plotted with a linear *y* axis.

in the 1.0-K experiments depends on the initial scale: the 400-km perturbation causes the greatest DTE growth, the 24-km perturbation causes the least growth, and the 1000-km perturbation causes intermediate growth. This scale dependence is consistent throughout the 36-h periods of both the 2LPV and CTSS experiments, including all of the individual 2LPV ensemble members. Second, the errors in the 1.0-K experiments are greater than those in the 0.01- and 0.1-K experiments throughout the 36-h forecast period, indicating that the 1.0-K perturbations are too large in magnitude to illustrate the system's intrinsic predictability.

Moist convection is the principal physical process by which errors grow in our experiments, which is consistent with previous idealized studies of moist baroclinic waves (Zhang et al. 2007; SZ16). This is shown by Fig. 8, which depicts the evolution of column-maximum DTE and surface pressure for individual members of the 2LPV ensembles with perturbation amplitudes of 0.1 K and scales of 24 and 1000 km. Figure 9 shows the same fields, but for the corresponding near-twin CTSS experiments.

The 36-h error growth is highly localized in physical space to regions of moist convection. In the first 12 h, the largest DTE values are primarily in convective areas along the cold front (Figs. 8a,d and 9a,b). During the next 12 h, the errors continue to grow the fastest along the cold and occluded fronts, although there is some growth beyond the convective regions. In the 2LPV experiments, this is most notable in areas of wave activity to the east of the low pressure center (Figs. 8b,e), while in the CTSS experiments this is most notable in the cloud shield ahead of the warm front (Figs. 9c,d). From 24 to 36 h, the errors continue to spread throughout both cyclones, but the largest DTE values remain confined to the cold and occluded fronts (Figs. 8c,f and 9e,f). This convection-dominated mode of error growth is consistent between simulations with different background KE spectral slopes in the mesoscale (2LPV vs CTSS) and between experiments with different initial-error scales (24 vs 1000 km).

If moisture is not included, the error growth is negligible over at least the first 36 h. This is illustrated by the dashed lines in Figs. 7b and 7e, which show the DTE time series for the dry CTSS experiments with perturbation amplitudes of 0.1 K and scales of 24 and 1000 km. The slow error growth in the absence of moisture is likely because the unbalanced perturbations radiate away as gravity waves rather than growing via

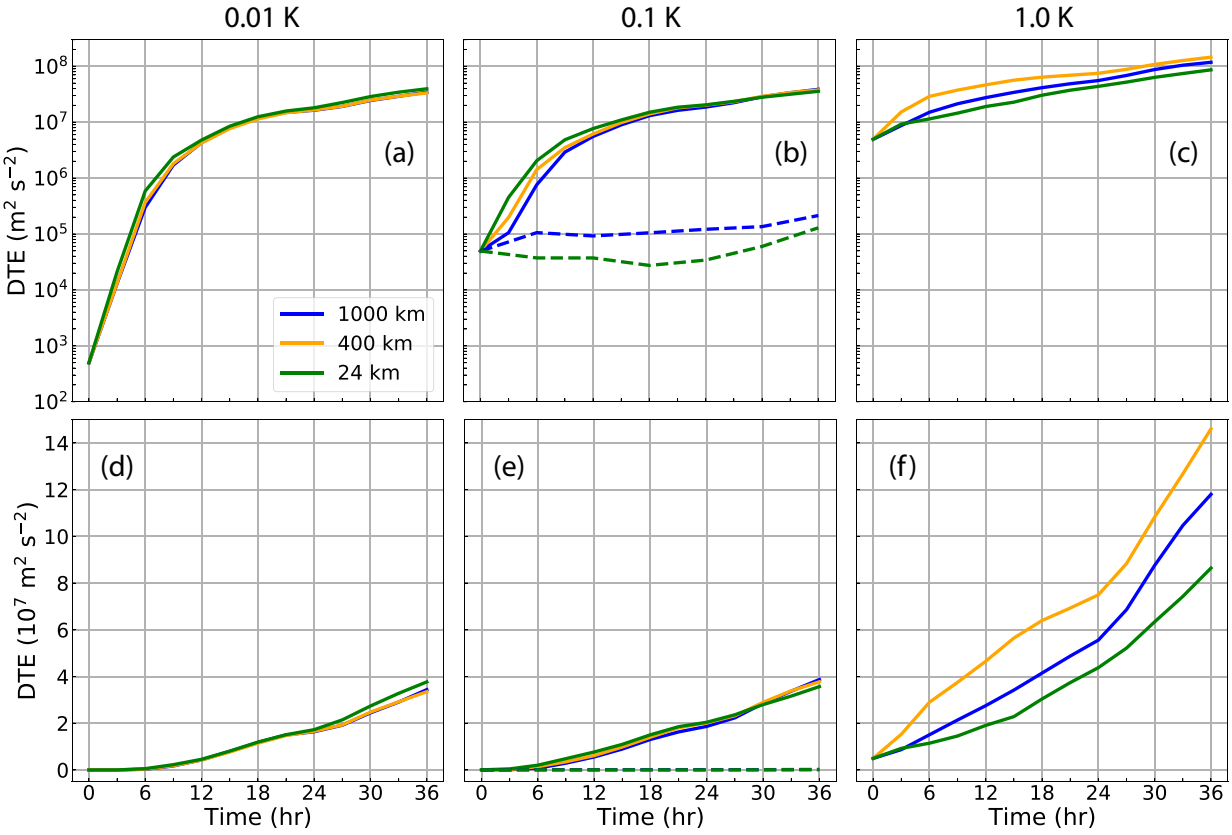

FIG. 7. As in Fig. 6, but for the near-twin CTSS experiments. The dashed lines in (b) and (e) refer to the dry experiments with initial perturbations at scales of 24 (green) and 1000 km (blue).

convective instability. By 36 h in the dry experiments, the only regions of nonnegligible column-maximum DTE are in areas of wave activity upstream of the cold front (Fig. 10). This further demonstrates the importance of moist processes in modulating the error growth in our baroclinic-wave simulations.

Given that the error growth is closely tied to moist convection, it is important to consider how much convective instability is present in each simulation. Figure 11a shows the meridional distributions of surface-based convective available potential energy (CAPE) for the 2LPV and CTSS background states; both exhibit strong conditional instability in the southern part of the domain, with the 2LPV case having more than twice the amount of CAPE as the CTSS case at the southern boundary. Notably, neither background state is as extreme as the control simulations of Tan et al. (2004) and Zhang et al. (2007) in which 6000 J kg^{-1} of CAPE is present at the southern boundary. The highest CAPE values in the southern portions of the 2LPV and CTSS domains, which are not representative of the values in midlatitude cyclones, remain well south of the low pressure centers. As shown in Figs. 11b and 11c, the CAPE is essentially zero throughout most of the area around both lows. Nonzero CAPE values do appear in the southern part of the warm sector, with values slightly larger than 1000 J kg^{-1}present at the leading edge of the cold front. Small patches of CAPE exceeding 100 J kg^{-1} are also as found as far north as the occluded front in the CTSS case. For comparison, CAPE values on the order of 1000 J kg^{-1} are observed along the warm conveyor belts of real-world midlatitude cyclones that produce intense convection (Oertel et al. 2021). Note that the areas with large column-maximum DTE (orange fill in Figs. 11b,c) extend well beyond the regions of moderately high CAPE. In summary, the 2LPV and CTSS simulations represent systems with very active convection, but the extremely large values of CAPE in the southern portions of the domains are not dominating the dynamics of either cyclone.

5. Error growth in spectral space

Thus far we have shown, using two families of baroclinic-wave simulations, that the growth of small-amplitude perturbations over a 36-h period is dominated by moist convection along frontal boundaries, regardless of the initial-error scale or the slope of the background KE spectrum. The goal of this section is to explore how the error growth manifests in spectral space. We will also contrast the error growth in our experiments with that of a 2D spectral turbulence model.

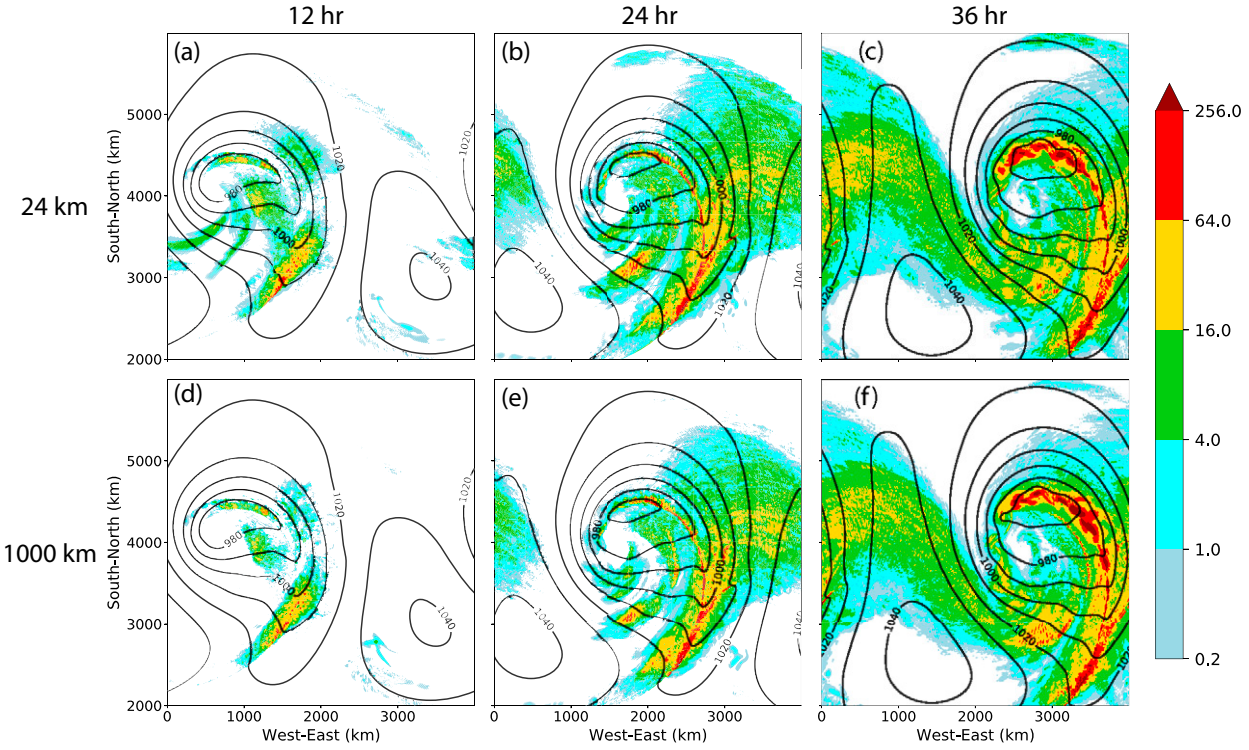

FIG. 8. Column-maximum DTE (color fill, $m^2\ s^{-2}$, as denoted by the nonlinear color bar) and surface pressure (black contours every 10 hPa) at (a),(d) 12, (b),(e) 24, and (c),(f) 36 h after initial errors are added for individual members of the 0.1-K 2LPV ensembles at scales of (a)–(c) 24 and (d)–(f) 1000 km.

a. Nonlocalized growth of error KE spectra

Figure 12 shows the evolution of midtropospheric 2D error KE spectra in the 0.01-K ensemble-mean 2LPV and near-twin CTSS experiments for the three perturbation scales. Error spectra are computed using (2), but with the velocities replaced by the differences between the velocities of the unperturbed and perturbed simulations. Time-averaged background KE spectra are also plotted after being multiplied by 2 to represent error saturation limits.

The error growth in the 0.01-K experiments is broad in spectral space, no matter the initial scale of the perturbation nor the slope of the background KE spectrum. In both the 2LPV and CTSS experiments, the monochromatic initial perturbations rapidly spread throughout all other scales such that the error KE spectra for the 24-, 400-, and 1000-km experiments are nearly identical at 3 h, aside from the remnants of peaks at the initial wavelengths. These peaks are mostly gone by 6 h as the errors continue to spread both upscale and downscale. Except at the wavelengths of the initial errors, the growth between 3 and 6 h is mostly up-amplitude in the sense that the error KE increases by roughly 1.5 decades at most wavelengths in all panels of Fig. 12. Such up-amplitude growth continues through the remainder of the 36-h forecast period at all wavelengths where the error remains unsaturated. This up-amplitude, nonlocalized growth in spectral space differs from the classical upscale cascade in which errors at a given scale remain negligible until errors at slightly smaller scales begin to saturate (see Fig. 15c). By 36 h in all 0.01-K experiments, the error is saturated at all wavelengths less than about 60 km, but it has similar or greater absolute magnitude at longer wavelengths up to roughly 1000 km.

The nonlocalized evolution of error KE spectra in our experiments might be expected given that the error growth is highly localized in physical space to regions of moist convection (Figs. 8 and 9). As emphasized by Durran et al. (2013), small-scale, localized perturbations in physical space appear broad and are maximized at large scales in spectral space. Spectrally broad, up-amplitude error growth has been observed in several other studies simulating realistic atmospheric flows (Mapes et al. 2008; Durran and Weyn 2016; Weyn and Durran 2017; Judt 2018, 2020).

In addition, the evolution of error KE spectra in the CTSS and 2LPV experiments are very similar, despite the two simulations having drastically different background KE spectral slopes in the mesoscale. This conflicts with predictions from turbulence theory suggesting that small-scale errors should grow and saturate faster in the 2LPV simulation because the mesoscale background KE spectral slope is shallower than in the CTSS simulation. In fact, the opposite is observed in our experiments: mesoscale errors approach saturation faster in the CTSS than the 2LPV experiments despite having a steeper background slope at those wavelengths.

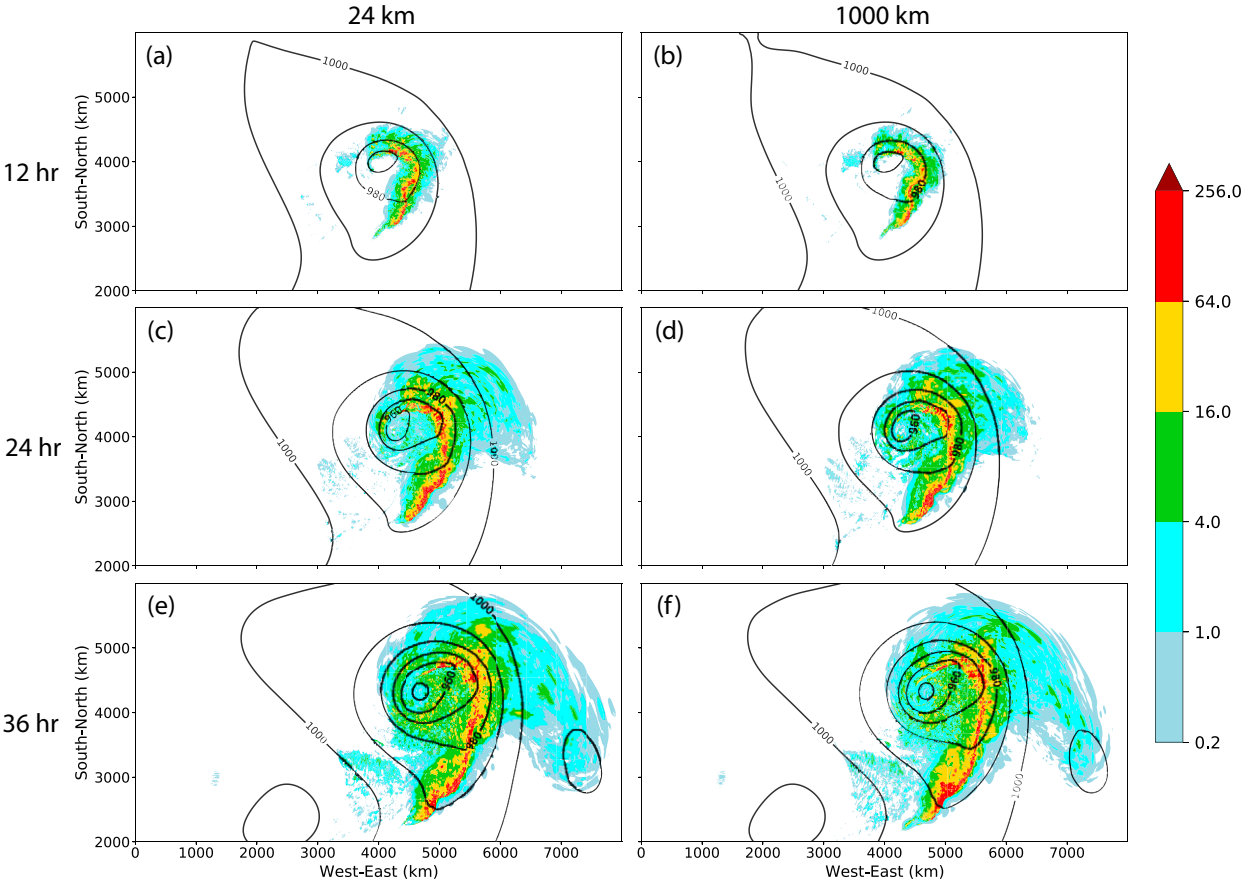

FIG. 9. As in Fig. 8, but for the 0.1-K near-twin CTSS experiments at (a),(b) 12, (c),(d) 24, and (e),(f) 36 h after initial perturbations are added at scales of (a),(c),(e) 24 and (b),(d),(f) 1000 km.

The more rapid mesoscale saturation in the CTSS experiments is illustrated by Fig. 13a, which shows the time series of the ratio of error to saturation midtropospheric KE, expressed as a percent, for the 0.01-K experiments over the 40–60-km wavelength range. This range is chosen because they are the largest wavelengths that reach 80% saturation by 36 h in all experiments, which we consider to be the threshold for significant predictability loss following Weyn and Durran (2017). Mesoscale errors saturate more rapidly in the CTSS experiments for all perturbation scales, reaching the 80% saturation threshold by 21 h. Meanwhile, errors in the 2LPV experiments do not reach 80% saturation until 36 h. Figure 13b demonstrates that this result is not a consequence of the perturbations being added at an earlier stage of the simulation in the CTSS case. When the 400-km perturbation is added at day 4.5 of the CTSS simulation (as in the 2LPV experiments),

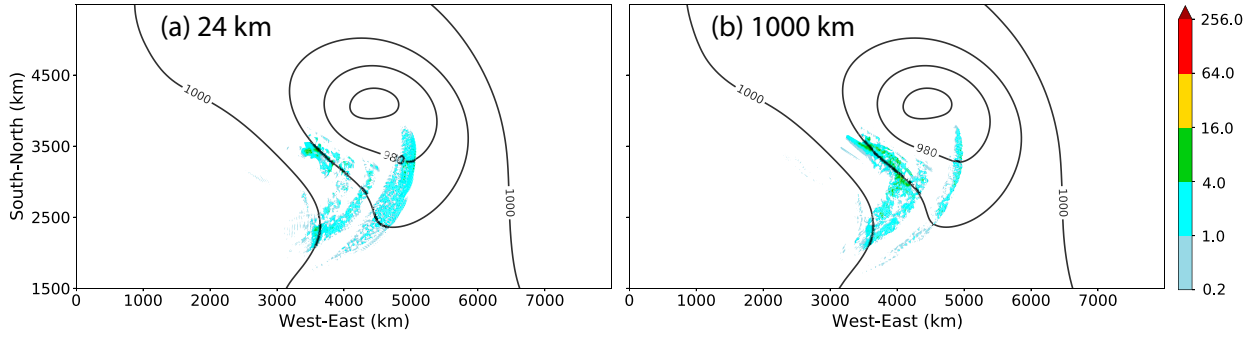

FIG. 10. As in Fig. 9, but for the dry 0.1-K CTSS experiments at 36 h after perturbations are added at scales of (a) 24 and (b) 1000 km.

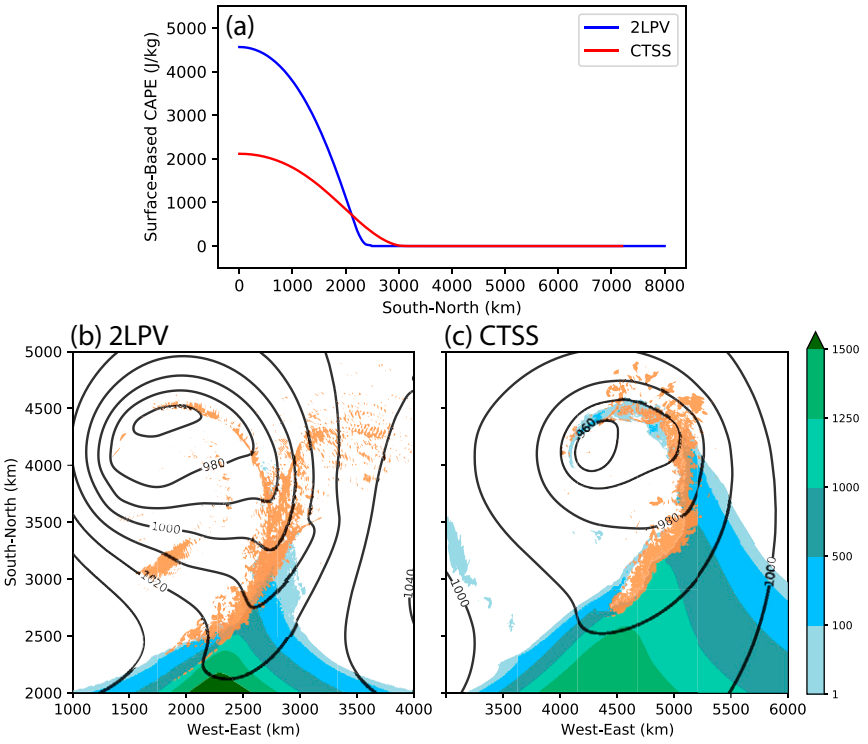

FIG. 11. (a) Meridional distributions of surface-based convective available potential energy (CAPE; J kg^{-1}) for the 2LPV (blue) and CTSS (red) background states. (b),(c) Surface-based CAPE (color fill, J kg^{-1}, as denoted by the nonlinear color bar) and surface pressure (black contours every 10 hPa) at 24 h after perturbations are added in the (b) 2LPV and (c) CTSS experiments with initial-error amplitudes of 0.1 K and scales of 24 km. The orange shading denotes where the column-maximum DTE exceeds 16 $m^2 s^{-2}$.

the time series of error saturation remains largely unchanged: mesoscale errors still saturate more rapidly than in the 2LPV experiments. These results demonstrate that spectral error growth on the mesoscale need not be faster when the slope of the background KE spectrum is shallower. In section 5b we will discuss why this result might be expected given that the errors grow nonlocally in spectral space.

Figure 14 shows the evolution of error KE spectra for the larger-amplitude 0.1- and 1.0-K CTSS experiments. Over the first 3 h, the errors in the 0.1-K experiments spread rapidly to other wavelengths and, except near the scale of the initial error, become largest at the shortest wavelengths. The 3-h growth is also faster if the initial perturbation is smaller in scale, which is consistent with the time series of domain-integrated DTE (Fig. 7b). This growth does not, however, take the form of a localized cascade upscale from the wavelength of the perturbation; instead, the faster growth occurs on all scales except at the initial-error wavelength. Beyond 3 h, up-amplitude growth continues such that the error spectra in all of the 0.1-K experiments are about equal at 6 h, except at the wavelengths of the initial perturbations. Between hours 12 and 36, the magnitude, distribution, and up-amplitude growth of the error spectra in the 0.1-K experiments are nearly identical to those in the 0.01-K experiments (cf. Figs. 12d–f). This is further evidence that our baroclinic-wave simulations have limited predictability and that this limit is not sensitive to the initial wavelength of the error nor to the slope of the background KE spectrum at that wavelength.

The 1.0-K CTSS experiments produce much greater errors than the smaller-amplitude cases during the 36-h forecast period, particularly at longer wavelengths. In the 24-km experiment, the error KE at the perturbation wavelength initially exceeds the background KE, which results in the nearly immediate saturation of the small scales and rapid growth at larger scales. Having overshot the background spectrum, the initial peak in error KE falls back to the saturation KE during the first 12 h. In contrast, the 400- and 1000-km perturbations do not overshoot the background spectrum, so the initial peaks in error KE are not forced to recede to the saturation KE. This leads to faster relative error growth at scales away from the initial wavelength beyond the first 3 h and is likely responsible for the greater domain-integrated DTE seen in the 400- and 1000-km experiments (Figs. 7c,e). The 36-h errors in all of the 1.0-K experiments are about an order of magnitude greater than those of the 0.01- and 0.1-K experiments at large scales where the error is unsaturated. The fact that decreasing the initial-error amplitude from 1.0 to 0.1 K leads to a significant decrease in the 36-h error KE at large scales further demonstrates that the 1.0-K perturbations are too large in amplitude to give an indication of the system's intrinsic predictability.

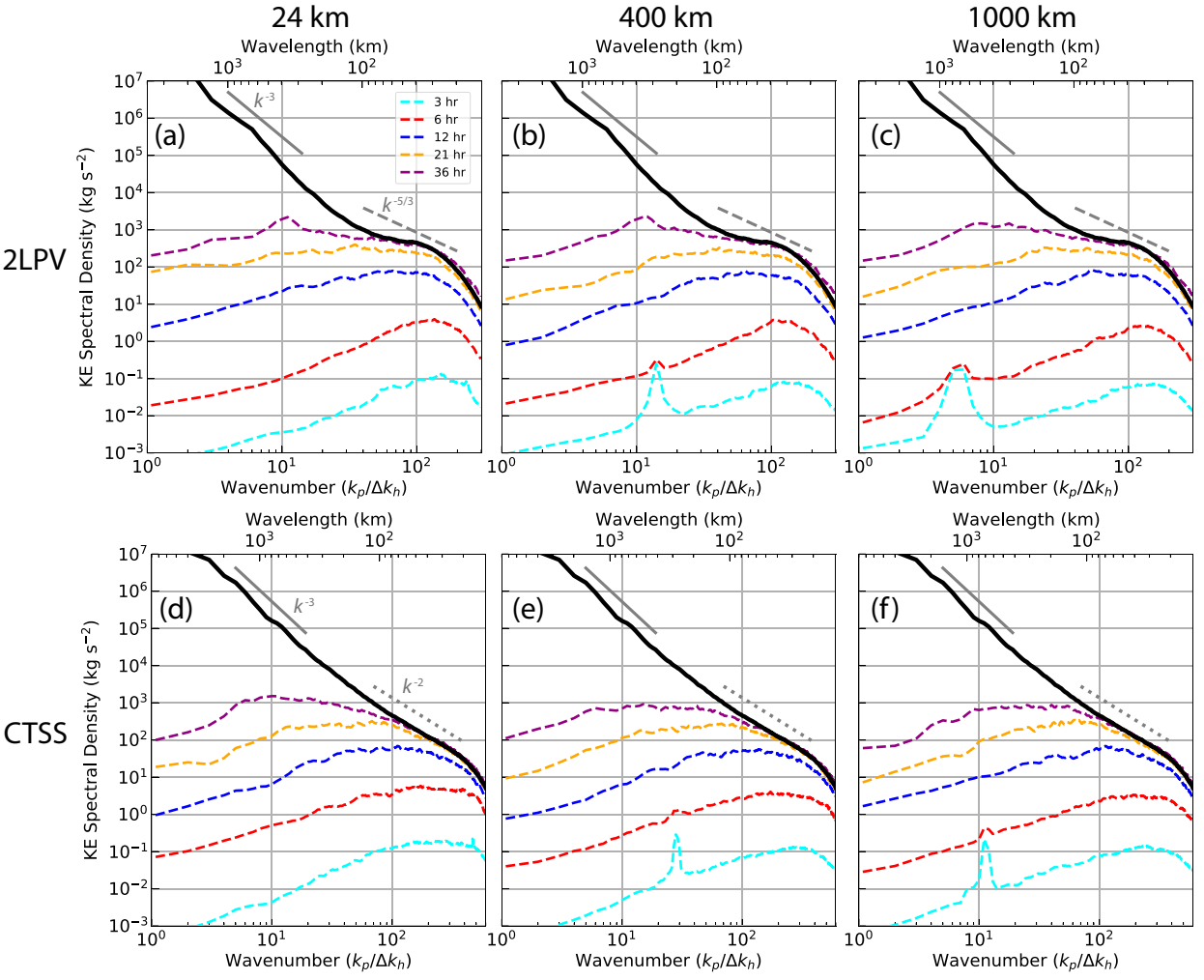

FIG. 12. Two-dimensional background (solid black) and error (dashed colors) KE spectral densities for the 0.01-K (a)–(c) 2LPV and (d)–(f) CTSS experiments with initial-error scales of (a),(d) 24, (b),(e) 400, and (c),(f) 1000 km. Error spectra are plotted at 3 (cyan), 6 (red), 12 (blue), 21 (orange), and 36 h (purple) after perturbations are added. Background spectra are averaged over the 36-h forecast periods and are multiplied by 2 to represent saturation limits. All spectra are averaged over the midtroposphere. The 2LPV spectra are averaged over their respective ensembles. Gray lines with slopes of k^{-3} (solid), $k^{-5/3}$ (dashed), and k^{-2} (dotted) are plotted for reference.

b. *Contrast with a spectral turbulence model*

Error growth in the Lorenz (1969) model of homogeneous turbulence in two-dimensional incompressible flow depends on the slope of the background KE spectrum through the presence of the background streamfunction field in the linearized governing equation. Numerical solutions to the Lorenz model show rapid upscale error growth and limited predictability when the slope of the background KE spectrum is shallower than k^{-3} (Rotunno and Snyder 2008).

Lorenz (1969), Lilly (1972), and Palmer et al. (2014) explained the dependence of error growth on the slope of the background KE spectrum by introducing a spectrally localized time scale $\tau(k)$ representing the time required for errors at wavenumber k to grow and contaminate the predictability at an adjacent scale having twice the wavelength. For a homogeneous multiscale turbulent flow, dimensional analysis implies that $\tau(k) \sim k^{-3/2}\tilde{E}(k)^{-1/2}$, where $\tilde{E}(k)$ is the background KE density per unit wavenumber (having units of m^3 s^{-2}). If the background KE spectrum follows a power law such that $\tilde{E}(k) = c_0 k^{-p}$, $\tau(k)$ is proportional to $k^{(p-3)/2}$. The time it takes for the predictability at a large scale k_L to be degraded by the upscale growth of initial errors beginning at a much smaller scale with wavenumber $2^N K_L$ scales as the sum of $\tau(k)$ over the N octaves from $2^N K_L$ to k_L,

$$T_L = \sum_{n=0}^{N} \tau\left(2^n k_L\right) = c_0^{-1/2} \sum_{n=0}^{N} \left(2^n k_L\right)^{(p-3)/2} = c_0^{-1/2} \frac{1 - \left[2^{(p-3)/2}\right]^{N+1}}{1 - 2^{(p-3)/2}} k_L^{(p-3)/2}. \quad (5)$$

If $p < 3$, the lead time T_L converges to a finite value as $N \to \infty$, implying that pushing the initial error to smaller and smaller scales does not extend the predictability horizon.

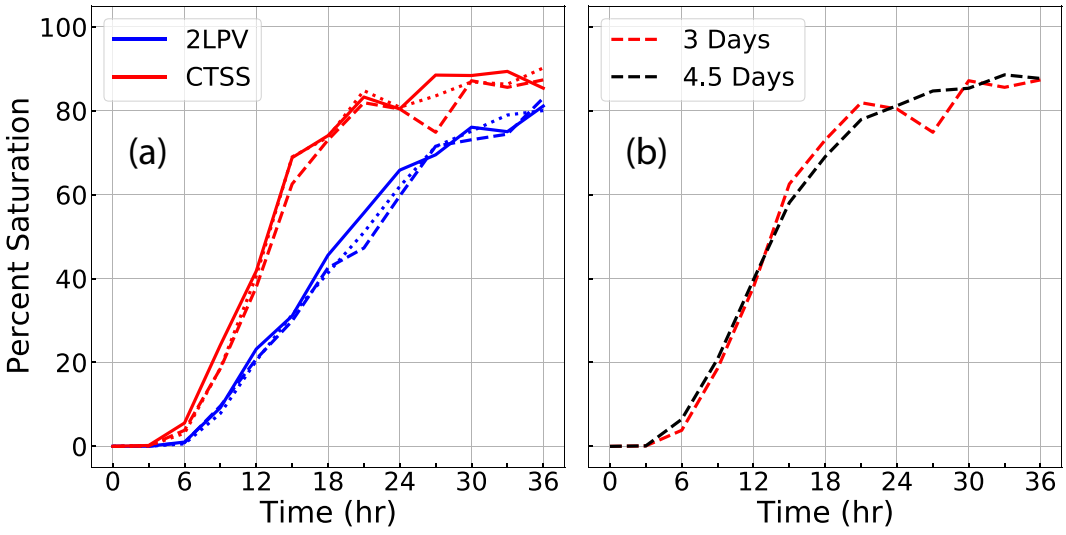

FIG. 13. Time series of error saturation (the ratio of error to saturation kinetic energy; %) summed over horizontal wavelengths of 40–60 km and averaged over the midtroposphere for (a) the 0.01-K CTSS (red) and ensemble-mean 2LPV (blue) experiments with initial-error scales of 24 (solid), 400 (dashed), and 1000 km (dotted) and (b) the 0.01-K, 400-km CTSS experiments with perturbations added at 3 (dashed red) and 4.5 days (dashed black).

Conversely, if $p \geq 3$, T_L diverges as $N \to \infty$, and the predictability horizon can, therefore, be progressively extended by continually reducing the scales subject to initial error.

For background KE spectra with the same c_0 and $p < 3$, the preceding scaling argument also implies that the shallower the slope (i.e., the smaller the p), the faster the error transfer across a given wavenumber, and the more limited the predictability. This is consistent with Lorenz (1969, Table 3), who found that, although the predictability limit remained finite, mesoscale errors grew more slowly in his experiment D with a background spectral slope of $k^{-7/3}$ than in the corresponding $k^{-5/3}$ case (e.g., experiment A).

Lorenz did note that this change in p only produced a modest 5% increase in the total time required to saturate the error at the longest wavelength (40 000 km) and observed that adjusting the value of c_0 to keep the total domain-integrated energy constant between experiments A and D essentially eliminated this 5% difference. He therefore hypothesized that for systems with $p < 3$ "the range of intrinsic predictability may depend mainly upon the total energy rather than on the details of the spectrum." This hypothesis certainly does not apply to the mesoscale error growth in his model, where, for example, he found that the time for errors to grow from a wavelength of 9.766–19.531 km increased from about 27 min to about 3.1 h as p increased from 5/3 to 7/3. As noted in Sun and Zhang (2020), the time required to saturate the errors in the largest scale in homogeneous turbulence models "has the same order of magnitude as the eddy turnover time at the largest scale." The background KE spectrum utilized by Lorenz sets the KE per unit logarithm of the wavenumber to zero at $k = 0$ and deviates from the mesoscale power spectrum such that the energy in wavenumbers 1–5 is identical in experiments A and D and dominates the total energy (his Table 1); therefore, his proposed rescaling does not come close to equalizing the error growth rates through the mesoscale.

Although the preceding scaling argument for the importance of the slope of $\tilde{E}(k)$ applies to Lorenz's model for homogeneous turbulence, it does not apply to our baroclinic-wave experiments because the circulations are very nonhomogeneous. The error growth is highly localized in physical space to regions of moist convection, and thus it is not localized in spectral space. Errors are transferred to a given scale from a broad range of wavenumbers. As a result, the evolution of the error spectra is not sensitive to the location of the initial perturbation in spectral space (i.e., its horizontal scale) nor to the slope of the background KE spectrum.

To emphasize this contrast between the error growth in our baroclinic-wave simulations and that of turbulence models, here we consider two additional 2LPV experiments run out to 3 h. As before, we perturb the potential temperature field at day 4.5 following (3), but with the phase shifts set to $\phi_x = \phi_y = 0$, resulting in near-twin simulations instead of ensembles. We add the perturbations at wavelengths of $L = 100$ km, which is in a region of the background KE spectrum where the slope is flat, and $L = 1000$ km, which is located under the steepest portion of the background spectrum (Fig. 5). For the sake of comparison with Lorenz's experiments, we use our smallest initial-error amplitude $A = 0.01$ K.

The turbulence model we use to compare with our baroclinic-wave experiments is the smooth-saturation Lorenz–Rotunno–Snyder (ssLRS) model described in Durran and Gingrich (2014). The ssLRS model can be configured with different background KE spectral slopes and with different underlying dynamics. We implement the ssLRS model using 24 wavenumbers that increase geometrically by powers of $2^{1/2}$.

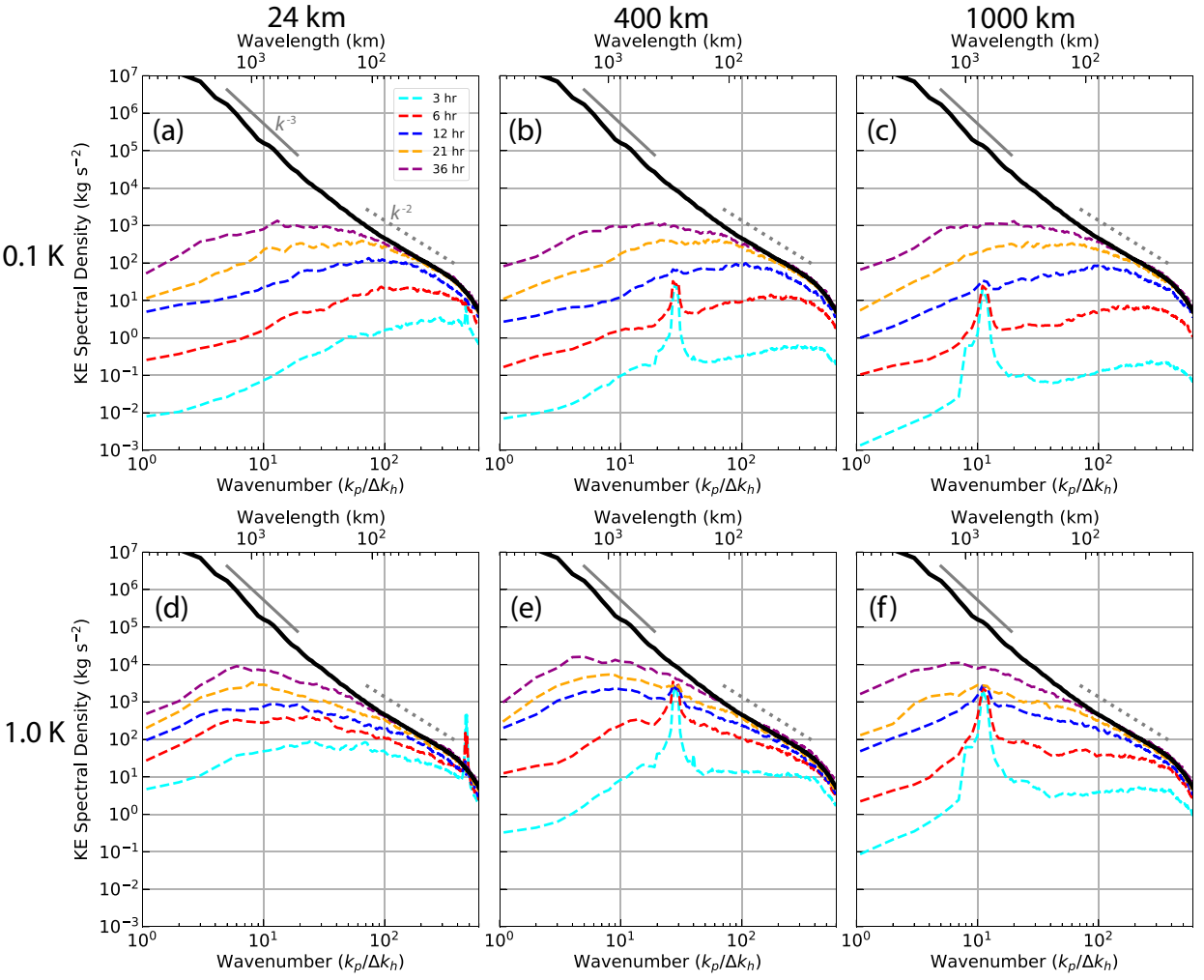

FIG. 14. As in Figs. 12d–f, but for the CTSS experiments with initial-error amplitudes of (a)–(c) 0.1 and (d)–(e) 1.0 K and initial-error scales of (a),(d) 24, (b),(e) 400, and (c),(f) 1000 km.

We dimensionalize our results such that the longest wavelength corresponds to the zonal domain size of the 2LPV simulation (4000 km). The time scale (and implicitly the value of c_0) is dimensionalized based on the observed KE spectral density of roughly $\tilde{E}_{400} = 2.5 \times 10^5$ m^3 s^{-2} at a wavelength of 400 km, which is approximately the scale at which the slope of the observed KE spectrum transitions from k^{-3} to $k^{-5/3}$ (Nastrom and Gage 1985) and is therefore a reasonable common point for background spectra with either of these slopes. The dimensionalized time scale then becomes $\tau = (k_{400})^{-3/2}(\tilde{E}_{400})^{-1/2}$, where $k_{400} = 2\pi/(400 \text{ km})$. The initial perturbation KE spectral density is defined to be very small at all scales except for the initial perturbation at a wavelength of just over 100 km.

Figure 15 depicts the evolution of error spectra in the 2LPV and ssLRS experiments. Figures 15a and 15b show the midtropospheric error KE spectra for the 2LPV experiments at 10, 30, 90, and 180 min after perturbations are added. The midtropospheric background KE spectrum plotted in black is averaged over the first 3 h and multiplied by 2 to represent the saturation limit. Figures 15c and 15d show the evolution of error KE spectra in two runs of the ssLRS model out to 180 min: one with surface quasigeostrophic dynamics (SQG) and a background KE spectrum proportional to $k^{-5/3}$, and another based on the two-dimensional barotropic vorticity equation (2DV) with $\tilde{E}(k)$ proportional to k^{-3}. Note that nonphysical negative error values develop at around 50 min; this is due to a flaw in Lorenz's original model that is discussed in appendix A of Weyn and Durran (2018) and likely arises from Lorenz's use of the quasi-normal approximation (Orszag 1970).

In the 2LPV experiments (Figs. 15a,b), the error growth is not sensitive to the slope of the background KE spectrum at the wavelength of the initial perturbation. The perturbations at 100 and 1000 km spread throughout all other scales during the first 3 h, resulting in the errors in the two experiments being about equal at those scales that are not adjacent to the peaks at the initial wavenumbers (as, for example, at wavenumber 20). The nonlocalized, up-amplitude evolution of the error spectra results in similar growth in the 100- and 1000-km

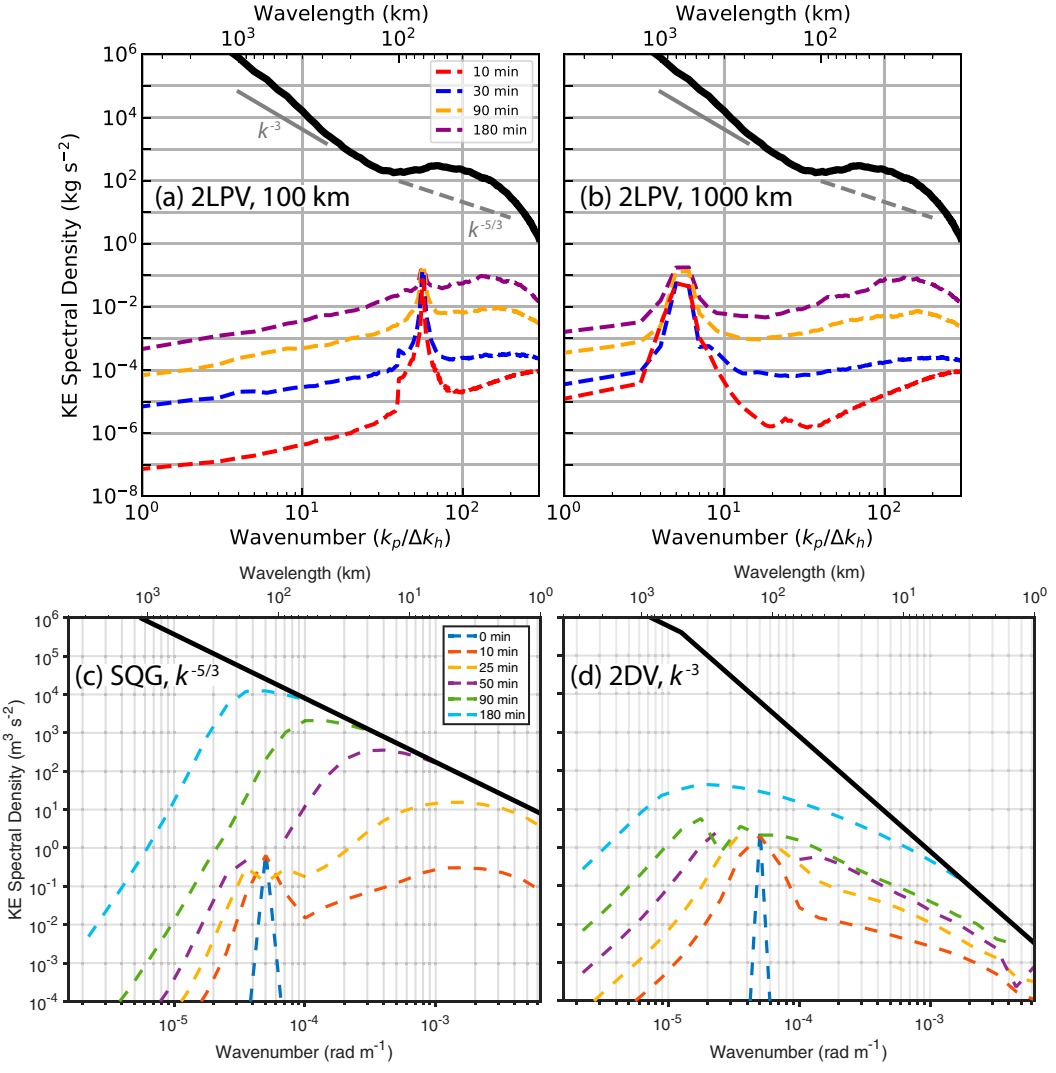

FIG. 15. (a),(b) As in Figs. 12a–c, but for the 0.01-K near-twin 2LPV experiments with initial-error scales of (a) 100 and (b) 1000 km. Error spectra are plotted at 10 (red), 30 (blue), 90 (orange), and 180 min (purple) after initial perturbations are added, and the background spectrum is averaged over the first 180 min and multiplied by 2 to represent the saturation limit. (c),(d) Background (solid black) and perturbation (dashed colors) KE spectral densities (m^3 s^{-2}) generated by the ssLRS model for (a) surface quasigeostrophic dynamics with a background slope of $k^{-5/3}$ and (b) the barotropic vorticity equation with a background slope of k^{-3}. Error spectra are plotted at 0 (blue), 10 (red), 25 (orange), 50 (purple), 90 (green), and 180 min (cyan).

experiments despite the initial errors appearing in regions of the background KE spectrum with drastically different slopes.

In contrast, upscale error growth in the ssLRS model (Figs. 15c,d) is dominated by interactions between adjacent wavelengths and is thus dependent on the slope of the background KE spectrum. In the SQG case with a $k^{-5/3}$ slope, errors grow much faster on small scales than on large scales, resulting in the rapid downscale spreading of error energy in the first 10 min and hardly any growth at scales larger than that of the initial perturbation. Just after 25 min, errors saturate at the smallest scales and an upscale cascade proceeds through the remainder of the first 3 h. This upscale cascade is not observed in any of our baroclinic-wave experiments, even those with initial perturbations in a region of the background KE spectrum where the slope is shallower than $k^{-5/3}$ (Fig. 15a). In the 2DV case with a steeper k^{-3} slope, small-scale errors grow no faster than large-scale ones, resulting in much slower growth than in the SQG run. The smallest scales in the 2DV run do not achieve saturation until about 3 h, by which time a broad large-scale maximum in error KE has developed.

c. One- versus two-dimensional error spectra

Do the preceding results based on 2D spectra change if instead we use one-dimensional (1D) spectral analysis? Durran et al. (2017) showed that if the 2D KE spectral density of a nondivergent, isotropic flow follows a k^{β} power law for $\beta < 0$, the 1D spectral density for that flow will follow the same power law, only with a different constant of proportionality (see also Leith 1971). Durran et al. (2017) also found this result to work well for divergent, anisotropic flows. The perturbation KE spectral slopes appearing in Fig. 12 do not, however, follow a k^{β} slope with some negative value for β. If they were to follow a power law, the corresponding β would be positive and thus the derivation in Durran et al. (2017) would not apply. Nevertheless, the literature on atmospheric predictability includes a mix of 1D (Mapes et al. 2008; Durran et al. 2013; Zhang et al. 2019; Judt 2020) and 2D (SZ16; Weyn and Durran 2017; Judt 2018; Weyn and Durran 2019) spectral analysis of error growth, without explicit discussion on the differences that might be expected between 1D and 2D spectral representations of the error.

The boundary conditions for the simulations used in this study allow either 1D or 2D spectral analysis. Here we compute perturbation KE spectra using both methods to identify the relationship between 1D and 2D error spectra in our experiments. The computation of 1D KE spectral densities in the zonal direction is straightforward in our simulations, as the domains are zonally periodic. Denoting the 1D discrete Fourier transform of a function ϕ by $\check{\phi}$ and its complex conjugate by $\check{\phi}^{*}$, the KE spectral density at each meridional grid point j and vertical level m is computed following Durran et al. (2017) as

$$E_{j,m}(k_x) = \frac{\bar{\rho}_m \Delta x}{2\pi N_x}\left[\check{u}_{j,m}(k_x)\check{u}^{*}_{j,m}(k_x) + \check{v}_{j,m}(k_x)\check{v}^{*}_{j,m}(k_x)\right]; \qquad (6)$$

$E_{j,m}(k_x)$ is then meridionally averaged to give the 1D KE spectrum at each vertical level. As in the 2D case, 1D perturbation KE spectra are also computed using (6), but with the velocities replaced by the differences between the velocities of the unperturbed and perturbed simulations.

Figure 16 shows the evolution of midtropospheric 1D and 2D error KE spectra for the CTSS experiment with an initial perturbation amplitude of 0.01 K and scale of 400 km. The time-averaged 1D and 2D background spectra are also plotted after multiplication by 2 to represent error saturation limits. The 1D and 2D background KE spectra have nearly identical slopes, which is consistent with previous studies (Durran et al. 2017).

The similarities between the 1D and 2D background spectral slopes do not, however, hold for the error spectra. The 1D error spectra are essentially flat throughout the 36-h forecast period, with equal perturbation KE at all wavelengths larger than the dissipative scales. In contrast, the 2D errors are largest at small scales and decrease with increasing wavelength. These differences are consistent with, for example, the differences between the flat 1D error spectra in Judt (2020) and the positively sloped 2D error spectra in Judt (2018). Nevertheless, the error growth using both computational methods is primarily up-amplitude, with relative errors growing at approximately the same rate at all scales, rather than through an upscale cascade.

6. Discussion and conclusions

In this study we investigate the sensitivity of mesoscale atmospheric predictability to the scale and amplitude of the initial disturbance, and to the slope of the background KE spectrum, using two families of convection-permitting idealized simulations of moist baroclinic waves. The first family of simulations examines error propagation in a midlatitude cyclone growing in a widely studied, but unrealistic, moist baroclinically unstable shear flow [the two-layer potential vorticity (2LPV) case]. The second family of simulations considers moist baroclinically unstable growth in a more realistic shear flow [the constant tropospheric static stability (CTSS) case]. After each cyclone undergoes a period of initial development, we perturb the low-level potential temperature fields at distinct wavelengths and amplitudes and examine how the errors induced by these perturbations evolve in physical and spectral space.

In our experiments with perturbation amplitudes of 0.01 and 0.1 K, the error growth is not sensitive to the initial horizontal scale up to 36-h lead times. About nine hours after their introduction, errors generated by the 0.01- and 0.1-K initial perturbations reach essentially the same amplitude and continue to produce similar error magnitudes for the remainder of the simulation. This insensitivity to the amplitude of the initial error suggests we are encountering intrinsic limitations on the predictability of the moist cyclogenesis in both the 2LPV and CTSS simulations. Similar insensitivities of the error growth to the scale of small-amplitude initial perturbations have been previously noted in studies of idealized models of homogeneous turbulence (Lorenz 1969; Durran and Gingrich 2014), in idealized and case-study simulations of organized convection (Durran and Weyn 2016; Weyn and Durran 2017, 2019), and in at least some experiments with moist baroclinically unstable waves (SZ16). In contrast to the 0.01- and 0.1-K experiments, the larger 1.0-K amplitude perturbations do produce greater error growth over the full period of each simulation and that growth is scale dependent, with the 400-km (24-km) initial perturbations producing the largest (smallest) errors.

We are not aware of previous studies documenting our other key finding, that error growth through the mesoscale in prototypical atmospheric disturbances is not sensitive to the slope of the background KE spectrum. This insensitivity is demonstrated by the nearly identical growth of errors initialized at wavelengths where the slope of the background KE spectrum is significantly different. For example, the error growth in the 2LPV simulation resulting from perturbations added where the background KE spectrum is flat is nearly identical to that produced when initial errors are added where the background slope is steeper than k^{-3} (Figs. 15a,b). Additionally, we find that small-scale errors in the CTSS simulation saturate faster than in the 2LPV case despite the CTSS case having a much steeper background KE spectral slope in the

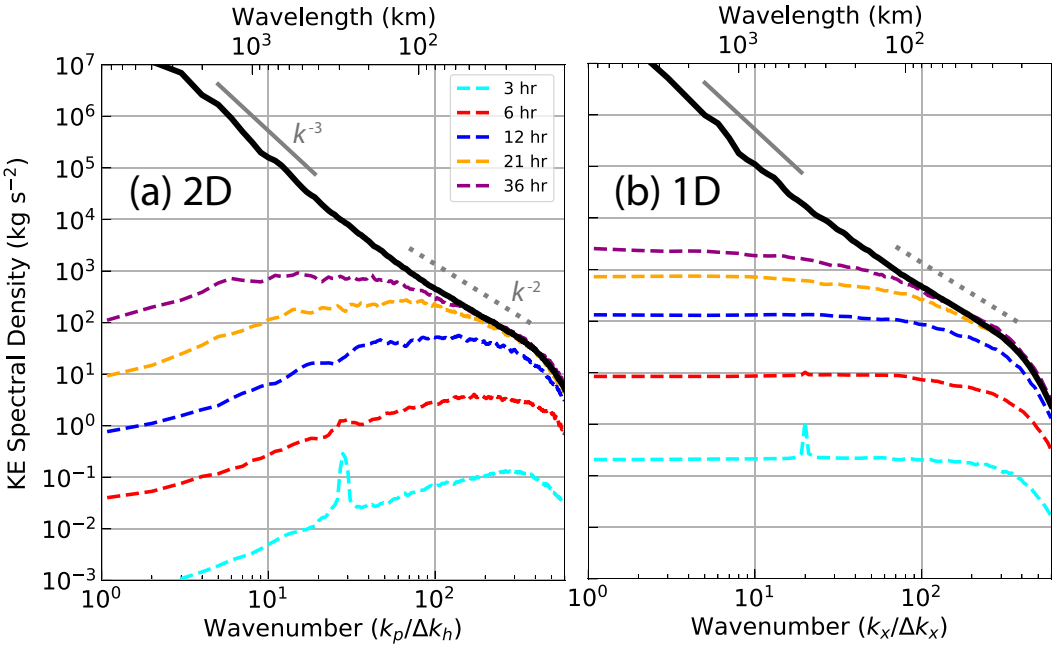

FIG. 16. (a) As in Fig. 12e, again computed using 2D spectra, and (b) meridionally averaged 1D spectra in the zonal direction, computed from the same data as in (a).

mesoscale (Fig. 13). This behavior is the opposite of what would be expected based on the dimensional analysis of error growth rates in homogeneous turbulence and the results obtained in idealized simulations by Lorenz (1969).

In contrast to idealized studies of error growth in homogeneous turbulence, the error growth in our experiments is highly localized in physical space to regions of moist convection. The idea that moist convection helps errors spread rapidly upscale is certainly not new (Zhang et al. 2003, 2007; Rodwell et al. 2013; Selz and Craig 2015), but key implications of the nonhomogeneous distribution of convection within midlatitude cyclones appear to have been overlooked. As apparent in Figs. 8 and 9, the convection and the largest errors are localized along the cold front. Such localized errors in physical space have a broad distribution in wavenumber (spectral) space, and therefore grow nonlocally in an up-amplitude fashion at all wavenumbers. The tendency of errors to grow up-amplitude, rather than cascade upscale in convection-permitting simulations of realistic atmospheric circulations was noted by Mapes et al. (2008), and has been reproduced in many subsequent studies. As demonstrated in Fig. 16, the shape of the error spectra undergoing such up-amplitude growth will depend on whether they are calculated using 1D or 2D Fourier transforms.

Since error growth is not localized in spectral space, it is not appropriate to make the dimensional analysis assumption that the error-growth time scale for a given wavenumber k is proportional to $k^{-3/2}E(k)^{-1/2}$, where $E(k)$ is the background kinetic energy. Error growth and the loss of mesoscale predictability in these moist midlatitude cyclone simulations is thereby decoupled from the slope of the background KE spectrum. It is possible that the limits to predictability may have some dependence on the slope of $E(k)$ in other atmospheric regimes where the dominant motions are more horizontally homogeneous, but there does not appear to be a universal relationship between atmospheric predictability and the slope of the background KE spectrum.

Because our simulations are conducted in a midlatitude f-plane channel, we are not able to realistically simulate error growth through the synoptic to the planetary scales. Previous research has consistently identified baroclinic instability as a key driver of extratropical error growth on these larger scales (Tribbia and Baumhefner 2004; Judt 2020). Analogous to the localized and anisotropic distribution of convection around midlatitude cyclones, the distribution of baroclinically unstable disturbances throughout the extratropics is not localized in spectral space, and it is therefore not obvious that a rigorous connection can be established between atmospheric predictability and the slope of the background KE spectrum on these larger scales. Future research could help clarify this question.

Acknowledgments. The authors are grateful for constructive reviews from Kerry Emanuel, Y. Qiang Sun, and an anonymous reviewer. This research was funded by Grants N00014-17-1-2660 and N00014-20-1-2387 from the Office of Naval Research and AGS 1929466 from the National Science Foundation. Author Lloveras was partly supported by a fellowship from the Achievement Rewards for College Scientists Foundation. High-performance computing support was provided on Excalibur, a supercomputer at the Army Research Laboratory DoD Supercomputing Resource Center (DSRC), on Conrad and Gordon, supercomputers at the Navy DSRC,

and by NCAR's Computational and Information Systems Laboratory on Cheyenne (doi:10.5065/D6RX99HX), sponsored by the National Science Foundation.

Data availability statement. The model input and output files used in this study are too large to publicly archive or to transfer. Instead, we provide all the information needed to replicate the simulations. The numerical model (WRF version 3.6.1) is publicly available at https://www2.mmm.ucar.edu/wrf/users/download/get_sources.html. The namelist settings for the WRF runs and the Python code for generating the WRF input files are archived with the University of Washington Libraries ResearchWorks repository: http://hdl.handle.net/1773/46944.

APPENDIX A

PV Formula for the CTSS Background State

We prescribe the CTSS background-state PV using the Exner function $\Pi = c_p(p/p_0)^{R_d/c_p}$ as the vertical coordinate, where p is the pressure, c_p = 1004 J K^{-1} kg^{-1} is the specific heat at constant pressure, R_d = 287 J K^{-1} kg^{-1} is the ideal gas constant for dry air, and p_0 = 1000 hPa is a reference pressure. The PV formula is

$$\mathrm{PV}(y,\Pi) = \frac{1}{2}(a\mathrm{PV}_T + b\mathrm{PV}_S) + \frac{1}{2}(a\mathrm{PV}_T - b\mathrm{PV}_S)\tanh\left(2\frac{\Pi - \Pi_{\mathrm{TP}}}{\Delta\Pi_{\mathrm{TP}}}\right), \tag{A1}$$

where PV_T = 0.22 PVU is the PV at the bottom of the troposphere and PVs = 1.8 PVU is the PV at the bottom of the stratosphere. The parameters a and b are

$$a(y,\Pi) = \begin{cases} 1 + 3\left(\dfrac{\Pi_0 - \Pi}{\Pi_0 - \Pi_{TP}}\right)^2 & \text{if } \Pi \geq \Pi_{\mathrm{TP}}, \\ 1 & \text{if } \Pi < \Pi_{\mathrm{TP}}, \end{cases} \tag{A2}$$

$$b(y,\Pi) = \begin{cases} 1 & \text{if } \Pi \geq \Pi_{\mathrm{TP}}, \\ 1 + 21\left(\dfrac{\Pi_{\mathrm{TP}} - \Pi}{\Pi_{\mathrm{TP}} - \Pi_{\mathrm{TOP}}}\right)^2 & \text{if } \Pi < \Pi_{\mathrm{TP}}, \end{cases} \tag{A3}$$

where Π_0 = 1004 J K^{-1} kg^{-1} is the Π value corresponding to the reference pressure p_0 = 1000 hPa and Π_{TOP} = 410 is the Π value at the top of the Π domain. The Π value at the tropopause Π_{TP} is defined as

$$\Pi_{\mathrm{TP}}(y) = \begin{cases} \Pi_m - \Delta\Pi_e & \text{if } \epsilon < -\dfrac{\pi}{2}, \\ \Pi_m + \Delta\Pi_e \sin(\epsilon) & \text{if } -\dfrac{\pi}{2} \leq \epsilon \leq \dfrac{\pi}{2}, \\ \Pi_m + \Delta\Pi_e & \text{if } \epsilon > \dfrac{\pi}{2}, \end{cases} \tag{A4}$$

where Π_m = 670 J K^{-1} kg^{-1} is the average Π value of the tropopause, $\Delta\Pi_e$ = 40 J K^{-1} kg^{-1} is the maximum deviation from the average tropopause Π value, $\epsilon = 2[y - (1/2)y_{\mathrm{tot}}]/\Delta y_e$, and Δy_e = 2500 km is the meridional scale for the tropopause transition.

APPENDIX B

CTSS Moisture Field

We add moisture to the CTSS background state by computing soundings at each horizontal grid point. First, we compute the saturation vapor pressure profile as

$$e_s = \begin{cases} 611.2\exp\left[17.67\left(\dfrac{T - 273.15}{T - 29.65}\right)\right] & \text{if } T > 273.15 \text{ K}, \\ 611.2\exp\left[21.87\left(\dfrac{T - 273.15}{T - 7.66}\right)\right] & \text{if } T \leq 273.15 \text{ K}. \end{cases} \tag{B1}$$

Next, we compute the water vapor mixing ratio profile q_v as

$$q_v = \mathrm{RH}_0 \frac{R_d}{R_v}\left(\frac{e_s}{p - e_s}\right), \tag{B2}$$

where p is the pressure profile, RH_0 = 0.75 is the reference relative humidity, R_d = 287 J K^{-1} kg^{-1} is the ideal gas constant of dry air, and R_v = 461.6 J K^{-1} kg^{-1} is the ideal gas constant of water vapor. Then we update the potential temperature profile using $\theta = \theta_v/(1 + 0.61q_v)$, where we assume that the potential temperature obtained through the PV inversion is equal to the virtual potential temperature θ_v. The new θ field is then used to rebalance the other input variables moist hydrostatically. This results in a relative humidity field that varies both meridionally and vertically, even though the relative humidity distribution is not prescribed explicitly.

REFERENCES

Bei, N., and F. Zhang, 2014: Mesoscale predictability of moist baroclinic waves: Variable and scale-dependent error growth. *Adv. Atmos. Sci.*, **31**, 995–1008, https://doi.org/10.1007/s00376-014-3191-7.

Bjerknes, J., 1919: On the structure of moving cyclones. *Mon. Wea. Rev.*, **47**, 95–99, https://doi.org/10.1175/1520-0493(1919)47<95:OTSOMC>2.0.CO;2.

Durran, D. R., and M. Gingrich, 2014: Atmospheric predictability: Why butterflies are not of practical importance. *J. Atmos. Sci.*, **71**, 2476–2488, https://doi.org/10.1175/JAS-D-14-0007.1.

——, and J. A. Weyn, 2016: Thunderstorms do not get butterflies. *Bull. Amer. Meteor. Soc.*, **97**, 237–243, https://doi.org/10.1175/BAMS-D-15-00070.1.

——, P. A. Reinecke, and J. D. Doyle, 2013: Large-scale errors and mesoscale predictability in Pacific Northwest snowstorms. *J. Atmos. Sci.*, **70**, 1470–1487, https://doi.org/10.1175/JAS-D-12-0202.1.

——, J. A. Weyn, and M. Q. Menchaca, 2017: Practical considerations for computing dimensional spectra from gridded data. *Mon. Wea. Rev.*, **145**, 3901–3910, https://doi.org/10.1175/MWR-D-17-0056.1.

Hong, S.-Y., and H.-L. Pan, 1996: Nonlocal boundary layer vertical diffusion in a medium-range forecast model. *Mon. Wea. Rev.*, **124**, 2322–2339, https://doi.org/10.1175/1520-0493(1996)124,2322:NBLVDI.2.0.CO;2..

——, Y. Noh, and J. Dudhia, 2006: A new vertical diffusion package with an explicit treatment of entrainment processes. *Mon. Wea. Rev.*, **134**, 2318–2341, https://doi.org/10.1175/MWR3199.1.

Jiménez, P. A., J. Dudhia, J. F. González-Rouco, J. Navarro, J. P. Montávez, and E. García-Bustamente, 2012: A revised scheme for the WRF surface layer formulation. *Mon. Wea. Rev.*, **140**, 898–918, https://doi.org/10.1175/MWR-D-11-00056.1.

Johnson, M., and Y. Jung, 2016: Comparison of simulated polarimetric signatures in idealized supercell storms using two-moment bulk microphysics schemes in WRF. *Mon. Wea. Rev.*, **144**, 971–996, https://doi.org/10.1175/MWR-D-15-0233.1.

Judt, F., 2018: Insights into atmospheric predictability through global convection-permitting model simulations. *J. Atmos. Sci.*, **75**, 1477–1497, https://doi.org/10.1175/JAS-D-17-0343.1.

——, 2020: Atmospheric predictability of the tropics, middle latitudes, and polar regions explored through global storm-resolving simulations. *J. Atmos. Sci.*, **77**, 257–276, https://doi.org/10.1175/JAS-D-19-0116.1.

Kishore, P., S. P. Namboothiri, K. Igarashi, J. H. Jiang, C. O. Ao, and L. J. Romans, 2006: Climatological characteristics of the tropopause parameters derived from GPS/CHAMP and GPS/SAC-C measurements. *J. Geophys. Res.*, **111**, D20110, https://doi.org/10.1029/2005JD006827.

Klemp, J. B., J. Dudhia, and A. D. Hassiotis, 2008: An upper gravity-wave absorbing layer for NWP applications. *Mon. Wea. Rev.*, **136**, 3987–4004, https://doi.org/10.1175/2008MWR2596.1.

Leith, C. E., 1971: Atmospheric predictability and two-dimensional turbulence. *J. Atmos. Sci.*, **28**, 145–161, https://doi.org/10.1175/1520-0469(1971)028<0145:APATDT>2.0.CO;2.

——, and R. H. Kraichnan, 1972: Predictability of turbulent flows. *J. Atmos. Sci.*, **29**, 1041–1058, https://doi.org/10.1175/1520-0469(1972)029<1041:POTF>2.0.CO;2.

Leung, T. Y., M. Leutbecher, S. Reich, and T. G. Shepher, 2020: Impact of the mesoscale range on error growth and the limits to atmospheric predictability. *J. Atmos. Sci.*, **77**, 3769–3779, https://doi.org/10.1175/JAS-D-19-0346.1.

Lilly, D. K., 1972: Numerical simulation studies of two-dimensional turbulence: II. Stability and predictability studies. *Geophys. Fluid Dyn.*, **4**, 1–28, https://doi.org/10.1080/03091927208236087.

Lin, Y.-L., R. D. Farley, and H. D. Orville, 1983: Bulk parameterization of the snow field in a cloud model. *J. Climate Appl. Meteor.*, **22**, 1065–1092, https://doi.org/10.1175/1520-0450(1983)022,1065:BPOTSF.2.0.CO;2.

Lorenz, E. N., 1969: The predictability of a flow which possesses many scales of motion. *Tellus*, **21A**, 289–307, https://doi.org/10.1111/j.2153-3490.1969.tb00444.x.

Lynch, P., 1997: The Dolph–Chebyshev window: A simple optimal filter. *Mon. Wea. Rev.*, **125**, 655–660, https://doi.org/10.1175/1520-0493(1997)125<0655:TDCWAS>2.0.CO;2.

Mansell, E. R., C. L. Ziegler, and E. C. Bruning, 2010: Simulated electrification of a small thunderstorm with two-moment bulk microphysics. *J. Atmos. Sci.*, **67**, 171–194, https://doi.org/10.1175/2009JAS2965.1.

Mapes, B., S. Tulich, T. Nasuno, and M. Satoh, 2008: Predictability aspects of global aqua-planet simulations with explicit convection. *J. Meteor. Soc. Japan*, **86A**, 175–185, https://doi.org/10.2151/jmsj.86A.175.

Menchaca, M. Q., and D. R. Durran, 2017: Mountain waves, downslope winds, and low-level blocking forced by a midlatitude cyclone encountering an isolated ridge. *J. Atmos. Sci.*, **74**, 617–639, https://doi.org/10.1175/JAS-D-16-0092.1.

——, and ——, 2019: The influence of gravity waves on the slope of the kinetic energy spectrum in simulations of idealized midlatitude cyclones. *J. Atmos. Sci.*, **76**, 2103–2122, https://doi.org/10.1175/JAS-D-18-0329.1.

Métais, O., and M. Lesieur, 1986: Statistical predictability of decaying turbulence. *J. Atmos. Sci.*, **43**, 857–870, https://doi.org/10.1175/1520-0469(1986)043<0857:SPODT>2.0.CO;2.

Nastrom, G. D., and K. S. Gage, 1985: A climatology of atmospheric wavenumber spectra of wind and temperature observed by commercial aircraft. *J. Atmos. Sci.*, **42**, 950–960, https://doi.org/10.1175/1520-0469(1985)042<0950:ACOAWS>2.0.CO;2.

Oertel, A., M. Sprenger, H. Joos, M. Boettcher, H. Konow, M. Hagen, and H. Wernli, 2021: Observations and simulation of intense convection embedded in a warm conveyor belt—How ambient vertical wind shear determines the dynamical impact. *Wea. Climate Dyn.*, **2**, 89–110, https://doi.org/10.5194/wcd-2-89-2021.

Orszag, S. A., 1970: Analytical theories of turbulence. *J. Fluid Mech.*, **41**, 363–386, https://doi.org/10.1017/S0022112070000642.

Palmer, T. N., A. Döring, and G. Seregin, 2014: The real butterfly effect. *Nonlinearity*, **27**, R123–R141, https://doi.org/10.1088/0951-7715/27/9/R123.

Rodwell, M. J., and Coauthors, 2013: Characteristics of occasional poor medium-range weather forecasts for Europe. *Bull. Amer. Meteor. Soc.*, **94**, 1393–1405, https://doi.org/10.1175/BAMS-D-12-00099.1.

Rotunno, R., and C. Snyder, 2008: A generalization of Lorenz's model for the predictability of flows with many scales of motion. *J. Atmos. Sci.*, **65**, 1063–1076, https://doi.org/10.1175/2007JAS2449.1.

——, W. C. Skamarock, and C. Snyder, 1994: An analysis of frontogenesis in numerical simulations of baroclinic waves. *J. Atmos. Sci.*, **51**, 3373–3398, https://doi.org/10.1175/1520-0469(1994)051<3373:AAOFIN>2.0.CO;2.

Selz, T., and G. C. Craig, 2015: Upscale error growth in a high-resolution simulation of a summertime weather event over Europe. *Mon. Wea. Rev.*, **143**, 813–827, https://doi.org/10.1175/MWR-D-14-00140.1.

Skamarock, W. C., and Coauthors, 2008: A description of the Advanced Research WRF version 3. NCAR Tech. Note NCAR/TN-475+STR, 113 pp., https://doi.org/10.5065/D68S4MVH.

——, S.-H. Park, J. B. Klemp, and C. Snyder, 2014: Atmospheric kinetic energy spectra from global high-resolution nonhydrostatic simulations. *J. Atmos. Sci.*, **71**, 4369–4381, https://doi.org/10.1175/JAS-D-14-0114.1.

Sun, Y. Q., and F. Zhang, 2016: Intrinsic versus practical limits of atmospheric predictability and the significance of the butterfly effect. *J. Atmos. Sci.*, **73**, 1419–1438, https://doi.org/10.1175/JAS-D-15-0142.1.

——, and ——, 2020: A new theoretical framework for understanding multiscale atmospheric predictability. *J. Atmos. Sci.*, **77**, 2297–2309, https://doi.org/10.1175/JAS-D-19-0271.1.

——, R. Rotunno, and F. Zhang, 2017: Contributions of moist convection and internal gravity waves to building the atmospheric −5/3 kinetic energy spectra. *J. Atmos. Sci.*, **74**, 185–201, https://doi.org/10.1175/JAS-D-16-0097.1.

Tan, Z.-M., F. Zhang, R. Rotunno, and C. Snyder, 2004: Mesoscale predictability of moist baroclinic waves: Experiments with parameterized convection. *J. Atmos. Sci.*, **61**, 1794–1804, https://doi.org/10.1175/1520-0469(2004)061<1794:MPOMBW>2.0.CO;2.

Tribbia, J. J., and D. P. Baumhefner, 2004: Scale interactions and atmospheric predictability: An updated perspective. *Mon. Wea. Rev.*, **132**, 703–713, https://doi.org/10.1175/1520-0493(2004)132<0703:SIAAPA>2.0.CO;2.

Waite, M. L., and C. Snyder, 2013: Mesoscale energy spectra of moist baroclinic waves. *J. Atmos. Sci.*, **70**, 1242–1256, https://doi.org/10.1175/JAS-D-11-0347.1.

Weyn, J. A., and D. R. Durran, 2017: The dependence of the predictability of mesoscale convective systems on the horizontal scale and amplitude of initial errors in idealized simulations. *J. Atmos. Sci.*, **74**, 2191–2210, https://doi.org/10.1175/JAS-D-17-0006.1.

——, and ——, 2018: Ensemble spread grows more rapidly in higher-resolution simulations of deep convection. *J. Atmos. Sci.*, **75**, 3331–3345, https://doi.org/10.1175/JAS-D-17-0332.1.

——, and ——, 2019: The scale dependence of initial-condition sensitivities in simulations of convective systems over the southeastern United States. *Quart. J. Roy. Meteor. Soc.*, **145** (Suppl. 1), 57–74, https://doi.org/10.1002/qj.3367.

Zhang, F., C. Snyder, and R. Rotunno, 2003: Effects of moist convection on mesoscale predictability. *J. Atmos. Sci.*, **60**, 1173–1185, https://doi.org/10.1175/1520-0469(2003)060<1173:EOMCOM>2.0.CO;2.

——, N. Bei, R. Rotunno, C. Snyder, and C. C. Epifanio, 2007: Mesoscale predictability of moist baroclinic waves: Convection-permitting experiments and multistage error growth dynamics. *J. Atmos. Sci.*, **64**, 3579–3594, https://doi.org/10.1175/JAS4028.1.

——, Y. Q. Sun, L. Magnusson, R. Buizza, S.-J. Lin, J.-H. Chen, and K. Emanuel, 2019: What is the predictability limit of midlatitude weather? *J. Atmos. Sci.*, **76**, 1007–1091, https://doi.org/10.1175/JAS-D-18-0269.1.